Effects of Coupling a Stochastic Convective Parameterization with Zhang-McFarlane Scheme on Precipitation Simulation in the DOE E3SMv1.0 Atmosphere Model

Yong Wang[1], Guang J. Zhang[2*], Shaocheng Xie[3], Wuyin Lin[4], George C. Craig[5], Qi Tang[3], Hsi-Yen Ma[3]

[1]Ministry of Education Key Laboratory for Earth System Modeling & Department of Earth System Science, Tsinghua University, Beijing, 100084 China
[2]Scripps Institution of Oceanography, La Jolla, CA, USA
[3]Lawrence Livermore National Laboratory, CA, USA
[4]Brookhaven National Laboratory, Upton, NY, USA
[5]Meteorologisches Institut, Ludwig-Maximilians-Universität, Munich, Germany

Submitted to *GMD*
July 28, 2020
Revised Feb 5, 2021

Corresponding author: Guang J. Zhang (gzhang@ucsd.edu), Scripps Institution of Oceanography, University of California San Diego, La Jolla, CA 92093.

Abstract. A stochastic deep convection parameterization is implemented into the U.S. Department of Energy (DOE) Energy Exascale Earth System Model (E3SM) Atmosphere Model version 1.0 (EAMv1). This study evaluates its performance on the precipitation simulation. Compared to the default model, the probability distribution function (PDF) of rainfall intensity in the new simulation is greatly improved. Especially, the well-known problem of “too much light rain and too little heavy rain” is alleviated over the tropics. As a result, the contribution from different rain rates to the total precipitation amount is shifted toward heavier rain. The less frequent occurrence of convection contributes to the suppressed light rain, while both more intense large-scale and convective precipitation contributes to the enhanced heavy total rain. The synoptic and intraseasonal variabilities of precipitation are enhanced as well to be closer to observations. The sensitivity of the rainfall intensity PDF to the model vertical resolution is examined. The relationship between precipitation and dilute convective available potential energy in the stochastic simulation agrees better with that in the Atmospheric Radiation Measurement (ARM) observations compared with the standard model simulation. The annual mean precipitation is largely unchanged with the use of the stochastic scheme except over the tropical western Pacific, where a moderate increase in precipitation represents a slight improvement. The responses of precipitation and its extremes to climate warming are similar with or without the stochastic deep convection scheme.

1. Introduction

Precipitation plays a vital role in the Earth's climate: the latent heat released during precipitation formation is a major energy source that drives the atmospheric circulation, and precipitation is an important part of the Earth's hydrological cycle. The accurate simulation of precipitation in global climate models (GCMs) is of great scientific and societal interest. However, GCMs used for current climate simulation and future projections suffer from many biases in the global distribution, frequency and intensity of simulated precipitation (Dai, 2006), which have negatively impacted the model's fidelity. Rainfall in nature is tightly associated with many complex dynamic and physical processes in the atmosphere, including large-scale circulation, convection, cloud microphysics, and planetary boundary layer (PBL) processes. The deficiencies in representing these processes in GCMs are prime culprits for errors in simulated rainfall (Watson et al., 2017).

Among the physical processes in GCMs, the parameterization of convection is responsible for some well-known biases: the double Intertropical Convergence Zone (Zhang and Wang 2006; Zhang et al., 2019), too weak synoptic and intraseasonal variabilities in the tropics (Zhang and Mu, 2005a; Watson et al., 2017), the wrong diurnal cycle of rainfall (Xie et al., 2019), "too much light rain and too little heavy rain" (Dai, 2006; Zhang and Mu, 2005b; O'Gorman and Schneider, 2009), to name a few. The conventional deterministic convective parameterization in GCMs represents the ensemble effects of subgrid-scale convective clouds in a model grid box on resolved scale variables. However, in reality, a given grid-scale state may lead to different realizations of subgrid-scale convection (Davies et al., 2013; Peters et al., 2013) rather than to a single "ensemble-mean" response. For instance, two model grid boxes, both in a similar convective-equilibrium state, can have different numbers and/or sizes of convective clouds due to stochasticity (Cohen and Craig, 2006). This stochasticity will appear more frequently as the model grid-box size becomes smaller (Jones and Randall, 2011). Not including stochasticity in convective schemes has been suggested to be at least partly responsible for the weak intraseasonal variability and "too much light rain and too little heavy rain" in GCMs (Lin and Neelin 2000, Wang et al., 2016; Watson et al., 2017; Peters et al., 2017).

As suggested in Palmer (2001, 2012), more realistic statistics of the impacts of subgrid convective clouds should be derived by simulating them as random samples from probability distributions conditioned on the grid-scale state, so that the influences of different individual realizations are introduced in the convection parameterization. In this regard, much effort in the past two decades has been made to develop stochastic convection schemes (e.g., Lin and Neelin, 2000, 2002; Plant and Craig, 2008; Khouider et al., 2010; Sakradzija et al., 2015). Among these schemes, Plant and Craig (2008) (PC08 hereafter) developed a stochastic deep convection parameterization under a framework based on statistical mechanics (Cohen and Craig, 2006; Craig and Cohen, 2006) for noninteracting convective clouds in statistical equilibrium using cloud-resolving model (CRM) simulations. This scheme was applied to numerical weather prediction (NWP) models and to a GCM in an aquaplanet setting, resulting in some substantial improvements in precipitation simulation (Groenemeijer and Craig, 2012; Keane et al., 2014, 2016).

Wang et al. (2016) incorporated the PC08 stochastic deep convection scheme into the Zhang-McFarlane (ZM) deterministic deep convection scheme (Zhang and McFarlane, 1995) in the National Center for Atmospheric Research (NCAR) Community Atmosphere Model version 5 (CAM5). They found that the introduction of the stochastic scheme improved the simulation of precipitation intensity and intraseasonal variability over the tropics in CAM5 (Wang and Zhang 2016; Wang et al., 2017).

In this study, we implement the PC08 stochastic deep convection parameterization scheme into the DOE Energy Exascale Earth System Model (E3SM) (Golaz et al. 2019) Atmosphere Model version 1.0 (EAMv1) (Rasch et al. 2019; Xie et al. 2018) and examine its effect on precipitation simulation. The EAMv1 is branched out from CAM5 and thus it inherits many model deficiencies from CAM5 as well. Many modifications in physics parameterizations have been made compared to CAM5 (Rasch et al. 2019; Xie et al. 2018). However, some model biases such as weak precipitation intensity persist (Xie et al. 2019). Thus, besides the precipitation metrics explored in our previous studies (Wang et al. 2016, 2017; Wang and Zhang 2016), this study will evaluate precipitation simulation with more systematical metrics. In addition, the responses of precipitation and its extremes to climate warming with the stochastic deep convection scheme will be investigated.

The organization of the paper is as follows. Section 2 presents parameterization, model, experimental design, and evaluation data. Section 3 describes results, including variability, frequency, intensity, amounts, duration, mean state, and responses of precipitation and its extremes to climate warming. The sensitivity of the rainfall intensity pdf to vertical resolution and underlying mechanisms are also presented in this section. Summary is given in section 4.

2. Parameterization, model, experimental design and evaluation data

2.1. Stochastic deep convection parameterization

The stochastic convective parameterization scheme of PC08 is modified for climate models when incorporating into the ZM deterministic deep convection scheme. The most essential part of the PC08 scheme involves two probability distributions. One is the probability distribution of mass flux of a cloud; it follows the exponential distribution:

$$p(m)dm = \frac{1}{\langle m \rangle} e^{-m/\langle m \rangle} dm \quad (1)$$

where <*m*> is the mean mass flux of a cloud and is a preset tuning parameter. The integral of the probability density over all values of mass flux is 1, i.e., probability one that every cloud has a mass flux between zero and infinity. The other is the probability of triggering *n* clouds for a given cloud mass flux in the range between *m* and *m*+d*m* at a given GCM grid box and time step; it is drawn from a Poisson distribution:

$$P_{\langle N \rangle}(n) = \frac{\langle N \rangle^n e^{-\langle N \rangle}}{n!} \qquad \text{for n=0, 1, 2, 3….} \quad (2)$$

where <*N*> is the ensemble mean number of convective clouds in the grid box. Here the sum of the probabilities over all *n* must equal one, i.e., probability one that some number between zero and infinity of clouds will be triggered with mass flux in this interval. Thus, the average number of clouds with mass flux between *m* and *m*+d*m*, $d\bar{n}(m)$, is:

$$d\bar{n}(m) = \langle N \rangle p(m)dm = \frac{\langle N \rangle}{\langle m \rangle} e^{-m/\langle m \rangle} dm \quad (3)$$

From eqs. (2) and (3), it follows then that for small $d\bar{n}(m)$ the probability of launching one convective cloud with mass flux between *m* and *m*+d*m* is given by:

$$p_{d\bar{n}(m)}(n = 1) = \frac{\langle N \rangle}{\langle m \rangle} e^{-m/\langle m \rangle} dm \quad (4)$$

Note that eq. (4) is not a probability density function, but rather the probability of triggering one cloud for a given cloud mass flux interval (*m*, *m*+d*m*), knowing that the average number of clouds within this mass flux interval is $d\bar{n}(m)$. <*N*>=<*M*>/<*m*>, where <*M*> is the ensemble mean total cloud mass flux given by the closure based on the convective quasi-equilibrium assumption in the ZM deterministic parameterization. For each mass flux bin, whether to launch a cloud is determined by comparing the probability $\frac{1}{<m>} e^{-\frac{m}{<m>}} dm$ with a random number uniformly generated between zero and one. Then, the sum of mass fluxes generated this way is multiplied by the factor <*N*> to rescale it to the mass flux of all clouds. The product of the total mass flux and the temperature and moisture tendencies form the bulk plume model gives the final temperature and moisture tendencies by the subgrid convective clouds.

There are two modifications to the original implementation in the NCAR CAM5. One is the update frequency of random numbers which, unlike the update frequency of once a day in Wang et al. (2016), is updated every 3 days in consideration of computational resources due to finer vertical and horizontal resolutions in the EAMv1 (see section 2.2). For the same reason, the spatial averaging of input quantities (i.e., vertical profiles of temperature and moisture) to the closure over neighboring grid points used in the original design of PC08 is not performed because it leads to an excessive communication load. One can argue that at a horizontal model resolution of about 110 km in EAMv1, convective quasi-equilibrium approximately holds over some timescale although at individual model timestep it does not. Thus, although spatial averaging is not applied, the temporal trailing averaging over 3 h at each time step is retained in the scheme. Other modifications to the PC08 scheme for incorporation into the ZM scheme in climate models (Wang et al. 2016) are retained. These include:

1) The temporally averaged quantities are used to calculate the ensemble mean cloud mass flux (<*M*>), which is determined by the ZM scheme. The unsmoothed grid point quantities are still used in the trigger function and the cloud model.

2) The root mean squared cloud radius information originally used in PC08 is not needed in our implementation because the ZM scheme does not use cloud radius.

3) The ensemble mean mass flux of a cloud <*m*> is set to 1×10^7 kg s^{-1} following Groenemeijer and Craig (2012).

4) The cloud life cycle effect with a factor d*t*/*T* (d*t* is the model time step and *T* is the constant lifetime parameter) in PC08 is not taken into account because the ZM deterministic parameterization does not consider the life cycle of convection.

2.2. EAMv1 model

The standard configuration of the DOE EAMv1 uses a spectral element dynamical core at a 110-km horizontal resolution on a cubed sphere geometry and a vertical resolution of 72 layers from the surface to 60 km (10 Pa) (Rasch et al. 2019, Xie et al. 2018). The treatment of PBL turbulence, shallow convection, and cloud macrophysics are unified with a simplified third-order turbulence closure parameterization CLUBB (Cloud Layers Unified by Binormals, Golaz et al., 2002; Larson and Golaz, 2005). The deep convection is represented by the ZM scheme. The Morrison and Gettelman (2008) (MG) microphysics scheme is updated to MG2 (Gettelman et al., 2015) with the prediction of rain and changes to ice nucleation and ice microphysics (Wang et al., 2014). A four-mode version of the modal aerosol module (MAM4) (Liu et a., 2016) is used with improvements to aerosol resuspension, aerosol nucleation, scavenging, convective transport and sea spray emissions for including the contribution of marine ecosystems to organic matter (Rasch et al., 2019). A linearized ozone chemistry module (Hsu and Prather, 2009; McLinden et al., 2000) is used to represent stratospheric ozone and its radiative impacts in the stratosphere. Other modifications for model tuning are provided in detail in Xie et al. (2018).

2.3. Experimental design

Six Atmospheric Model Intercomparison Project (AMIP) type simulations are conducted. Four 6-year simulations are forced by prescribed, seasonally varying climatological present-day sea surface temperatures (SSTs) and sea ice extent, recycled yearly (Stone et al., 2018): two with the default deterministic ZM scheme but having 72 and 30 vertical levels respectively (referred to as EAMv1 and EAMv1-30L) and the other two with the stochastic deep convection scheme (referred to as STOCH and STOCH-30L). The simulations with 30 vertical levels are conducted to facilitate the comparison with Wang et al. (2016), in which the vertical resolution of CAM5 is 30 levels (see section 3.3). To explore the responses of precipitation and its extremes to climate warming, similar to EAMv1 and STOCH runs, two 3-year simulations in a warmer climate are conducted, in which a composite SST warming pattern derived from the Coupled Model Intercomparison Project Phase 3 (CMIP3) coupled models (referred to as EAMv1-4K and STOCH-4K respectively) is imposed for the boundary condition of the atmosphere. Following Webb et al. (2017), it is a normalized multi-model mean of the sea surface temperature response pattern from 13 CMIP3 atmosphere-ocean general circulation models, representing the change of SST between years 0-20 and 140-160, the time of CO_2 quadrupling in the 1% runs. Before calculating the multi-model ensemble mean, the SST response of each model was divided by its global mean and multiplied by 4K. This guarantees that the pattern information from all models is weighted equally and that the global mean SST forcing is +4K warming. The first year in all simulations is discarded as a spin-up. Information for all experiments is summarized in Table 1.

2.4. Evaluation data

For model evaluation, the following datasets are used: The Clouds and the Earth's Radiant Energy System Energy Balanced and Filled (CERES-EBAF) (Loeb et al., 2009) for evaluation of shortwave and longwave cloud radiative forcing; the Interim European Centre for Medium-Range Weather Forecasts Re-Analysis (ERAI) (Simmons et al.,2007) for sea level pressure, zonal wind, relative humidity, specific humidity, and temperature; the European Remote Sensing Satellite Scatterometer (ERS) (Bentamy et al., 1999) for surface wind stress; and the Willmott-Matsuura (Willmott) (Willmott & Matsuura, 1995) data for land surface air temperature.

The rainfall mean state is evaluated against the Global Precipitation Climatology Project (GPCP) monthly product (version 2.1) at a resolution of 2.5^o (Adler et al., 2003; Huffman et al., 2009) while a daily estimate of GPCP version 1.2 at 1^o horizontal resolution (GPCP 1DD) (Huffman et al., 2001, 2012) is used for evaluation of precipitation amount distribution. In addition to GPCP, the Xie-Arkin pentad observations at 2.5^o resolution (Xie and Arkin, 1996) and the Tropical Rainfall Measuring Mission 3B42 version 7 (TRMM) daily observations at a resolution of 0.25^o over (50^oS, 50^oN) (Huffman et al., 2007) are applied to evaluate the precipitation variance. The TRMM data are also used in the PDF of rainfall intensity and the rainfall amount distribution. To estimate the uncertainty in the PDF of precipitation intensity in observations, additional daily rainfall products are used. These include TAPEER v1.5, GSMAP-NRT-gauges v6.0, PERSIANN CDR v1, CMORPH v1.0 CRT from the Frequent Rainfall Observation on GridS (FROGS) database (Roca et al., 2019) and GPM IMERG v06b (Huffman et al., 2017). For the rainfall duration evaluation, the TRMM 3B42 v7 3-hourly data is used. To make the comparison consistent between observations and model simulations, the model data with the same output frequency to that in the corresponding observations/reanalysis data are used and all observations/reanalysis data are regridded to the same 1^o lat-lon grids as EAMv1. The US Department of Energy Atmospheric Radiation Measurement (ARM) multi-year observations for daily precipitation and dilute convective available potential energy (CAPE) over the Southern Great Plains (SGP) site for the time period of 2004-2018 (Xie et al. 2004) and Green Ocean

Amazon (GOAmazon) field campaign (Martin et al. 2016) site for 2014-2015 (Tang et al. 2016) are used to evaluate the simulated CAPE vs. precipitation relationship.

3. Results

3.1. Intraseasonal and synoptic variability

The simulated variability of precipitation is an important aspect of model performance. Here we focus on intraseasonal and synoptic-scale variability. The intraseasonal variability associated with Madden-Julian oscillations (MJO) is problematic in many GCMs (Jiang et al. 2015; Zhang and Mu 2005). Figure 1 shows the tropical distribution of the 20-80 day intraseasonal variance for the total precipitation in observations and simulations. The variance is obtained with a Lanczos band-pass filter at each grid point. Both Xie-Arkin and TRMM observations show large variance in the Indian Ocean and western Pacific as well as in the ITCZ and the South Pacific Convergence Zone (SPCZ) regions. The intraseasonal variance in EAMv1 is much weaker, as in many other GCMs. Similar to the results in Wang et al. (2016), the STOCH run with the stochastic deep convection scheme has a significantly enhanced intraseasonal variance in these regions, making it much more comparable to observations although there is excessive precipitation variance over central Africa, the Himalayas, the Maritime Continent and the region near the Colombian coast. Compared with the EAMv1 run, the STOCH run has more small-scale noise in the spatial structure of the precipitation variability.

Besides the intraseasonal variance, the synoptic variance (2-9 day Lanczos band pass-filtered rainfall anomalies) is also investigated (Fig. 2). The synoptic-scale variance corresponds to weather activities. In Fig. 2 only TRMM observations are shown to evaluate simulations because the Xie-Arkin observations are pentad data. In TRMM, the geographical distribution of the synoptic variance is similar to that of the intraseasonal variance, but with larger amplitudes because synoptic-scale activities contain much more energy than intraseasonal disturbances. Similar to the intraseasonal variance, the synoptic variance in the EAMv1 run is also much weaker than that in observations. The synoptic-scale variance in the STOCH run is about twice as strong as in EAMv1 although it is still underestimated compared to TRMM observations. Over regions where the overestimated intraseasonal precipitation variance emerges, the STOCH run has excessive synoptic precipitation variance as well. This result is consistent with Goswami et al. (2017), which reported enhanced intraseasonal and synoptic variability of precipitation in the National Centers for Environmental Predictions (NCEP) Climate Forecast System version 2 (CFSv2) using a stochastic multicloud model parameterization.

3.2. Rainfall frequency, intensity, amount and duration

Wang et al. (2016) showed that the most significant improvement with the use of the stochastic deep convection scheme in CAM5 was in the simulated PDF of rainfall intensity over the tropics, which became very close to TRMM observations. Since there are many modifications in model configuration and physics parameterizations from CAM5 to EAMv1 (Rasch et al. 2019), such as a finer vertical resolution, an updated microphysics parameterization (MG2), and the use of CLUBB in place of separate shallow convection and planetary boundary layer turbulence parameterizations, it is not clear whether a similar degree of improvement in precipitation intensity PDF can be achieved with a similar stochastic convection scheme. Using an equal-interval rainfall intensity bin of 0.5 mm d^{-1} from 0 to 200 mm d^{-1}, Fig. 3 shows the frequencies of the total precipitation intensity over the tropics (20^{o}S-20^{o}N) from observations, EAMv1 and STOCH, respectively. Also shown are the PDFs of large-scale and convective precipitation intensity. The observational uncertainty is larger for intense precipitation than for light precipitation (Fig. 3a), which is consistent with findings in Roca (2019). The GPCP precipitation intensity distribution (the gray curve that even falls below the EAMv1 curve in Fig. 3a) has the lowest frequency for precipitation intensity greater than 30 mm d^{-1}. The GPCP product is known to have underestimated precipitation intensities (Kooperman et al., 2016). Despite the uncertainties in observations, the simulated frequencies in STOCH are more consistent with those in the ensemble mean of all observations than those in the default EAMv1. The stochastic convection parameterization in the STOCH run greatly mitigates the bias of "too much light rain and too little heavy rain", showing a decrease of the frequency of rainfall intensity between 1 and 10 mm d^{-1} and an increase of that of rainfall intensity larger than 20 mm d^{-1} compared to the EAMv1 run. Especially for light rain, the frequencies in STOCH fall in the observational range while those in EAMv1 do not. A recent study finds that the decreased frequency of light rain has a profound impact on simulated aerosol loading in the atmosphere (Wang et al. 2021). Xie et al. (2019) indicated that the "too much light rain" in EAMv1 was a result of too frequent convection. Consistent with this notion, Fig. 3b shows that the reduction of the light rain frequency is entirely from convective precipitation. On the other hand, the increase of intense precipitation frequency is from both convective and large-scale precipitation.

To understand why the use of stochastic convection scheme decreases the frequency of light rain and increases the frequency of heavy rain, we conducted an additional simulation. In the simulation, the setup is identical to the STOCH run except that the ZM scheme is called a second time at each time step, with input (temperature, moisture, etc.) identical to that for the stochastic scheme. However, the output is used for diagnostic purposes only and does not participate in model integration. It is found that (figure not shown) two factors contribute to the decreased frequency of light rain and increased frequency of heavy rain. First, for a given ensemble mean convective mass flux (from the ZM scheme) the probability for cloud generation following the Poisson distribution for a realization in the stochastic scheme can produce more intense precipitation than obtained by the ZM scheme. Second, the probability distribution results in less frequent convection in general. This allows the buildup of the atmospheric instability (also see Fig. 9 below in section 3.3), which also leads to heavier convective rainfall (even with ZM scheme alone without considering the stochastic part) as well as more large-scale condensation. However, we note that the increase of the frequency in rainfall intensity ranges from 60 to 140 mm d^{-1} in the STOCH run is not as much as that in Wang et al. (2016) for CAM5. This will be elucidated through sensitivity experiments in the next subsection.

The frequencies of total precipitation intensity over selected regions also show qualitatively similar degree of improvement. Fig. 4 shows six regions during their convectively active seasons: Amazonia, tropical western Pacific, India for June-September, Maritime Continent, SGP for May-August and eastern China for June-August in TRMM, EAMv1 and STOCH, respectively. In all tropical regions, the EAMv1 simulation overestimates the occurrence frequency for precipitation intensities less than 20 mm day^{-1} and underestimates it for precipitation intensities greater than 20 mm day^{-1}, similar to the distribution for the entire tropics. In STOCH, the performance in the pdf over Amazonia and Maritime Continent is better than the pdf over the entire tropics. Although the biases of “too much light rain” over India and tropical western Pacific are alleviated by the stochastic deep convection scheme, the bias of “too little heavy rain” remains, particularly over India where large-scale monsoonal dynamics regulate heavy convective rain (Wang et al., 2018). For the two midlatitude convection regions (SGP and eastern China), although there is also noticeable improvement across the precipitation intensity spectrum, it is less significant compared to other regions, possibly because convection in midlatitude land regions is not as prevalent as in the tropics.

Figure 5 shows the geographical distributions of precipitation frequency for all precipitation, for precipitation intensities less than 20 mm d^{-1}, and more than 20 mm d^{-1}, respectively, over the tropics in observations and simulations (days with precipitation intensity less than 1 mm d^{-1} are considered non-precipitating and thus excluded). In TRMM, the occurrence frequency of rainy days ranges from 30 to 70% with the most frequent rain along the ITCZ, the SPCZ and in the Indian Ocean, where the EAMv1 run has as high a frequency as 80-90%, with up to 30% positive biases. In contrast, the STOCH run reduces the frequency to 50-70% although it is still overestimated. When the total precipitation is broken down into precipitation rates less than 20 mm d^{-1} and precipitation rate above 20 mm d^{-1}, in both observations and simulations the geographical distribution of the rainy days is dominated by that of days with precipitation intensity less than 20 mm d^{-1}. In comparison with observations, again, the STOCH run reduces the positive bias of the frequency of precipitation intensity less than 20 mm d^{-1} in the EAMv1 run by up to 20%. For precipitation intensities greater than 20 mm d^{-1}, the EAMv1 run underestimates their frequency compared to the TRMM observations. On the other hand, the frequency of occurrence in the STOCH run is comparable to the TRMM observations.

Another metric for the precipitation pdf is the contribution of precipitation within a given intensity bin to the total precipitation amount. It combines the information of precipitation frequency distribution and precipitation intensity. While drizzle occurs much more frequently than the more intense rain events, it may not contribute much to the total precipitation amount. Following the approach of Kooperman et al. (2016, 2018), we divide the precipitation rate ranging from 0.1 to 1000 mm d^{-1} into equal bin intervals on a logarithmic scale, with a bin width of $\Delta \ln(R) = \Delta R/R = 0.1$. If the frequency of rainfall rates falling into the *i*th bin is denoted f_i, then $f_i = n_i/N_t$, where N_t is the total number of days, n_i is the number of days with rainfall rates falling into the *i*th bin. The mean precipitation rate in the *i*th bin is then:

$$R_i = \frac{1}{n_i}\sum_{j=1}^{n_i} r_j, \quad (5)$$

where r_j is an individual precipitation rate within the *i*th bin. Thus, the contribution to the total precipitation amount from the *i*th bin per unit bin width is given by:

$$P_i = \frac{f_i R_i}{\Delta \ln(R)} = \frac{1}{\Delta \ln(R)} \frac{1}{N_t} \sum_{j=1}^{n_i} r_j \quad (6)$$

P_i has the units of mm d^{-1}. The total precipitation amount is then given by:

$$P = \sum_i P_i \, \Delta \ln(R) = \sum_i f_i \, R_i \quad (7)$$

Accordingly, the amount distributions for total (P^T), convective (P^C) and large-scale (P^L) rainfall are given by:

$$P_i^T = \frac{1}{\Delta \ln(R)} \frac{1}{N_t} \sum_{j=1}^{n_i} r_j^T \quad (8)$$

$$P_i^C = \frac{1}{\Delta \ln(R)} \frac{1}{N_t} \sum_{j=1}^{n_i} r_j^C \quad (9)$$

$$P_i^L = \frac{1}{\Delta \ln(R)} \frac{1}{N_t} \sum_{j=1}^{n_i} r_j^L \quad (10)$$

where r^T, r^C and r^L are the total, convective and large-scale rain rates.

Figure 6a shows the contribution to the total rainfall amount from each rainfall rate on a logarithmic scale for GPCP 1DD, TRMM, and the two simulations, respectively, over the tropics. The TRMM observations have larger contributions from intense rainfall rates than GPCP 1DD, with the peak contribution rainfall rate of 28 mm d^{-1}, higher than the value of 22 mm d^{-1} in GPCP 1DD. The EAMv1 run produces a much smaller peak contribution rainfall rate (15 mm d^{-1}) than the two observations while the STOCH run simulates it realistically (23 mm d^{-1}), falling in between the two observations. Note that precipitation from intensities less than 1 mm d^{-1} contributes about 0.05 mm d^{-1} or less to the tropical mean total precipitation, thus justifying treating it as non-precipitating in Fig. 5. Fig. 6b shows the convective and large-scale contributions to the simulated total precipitation from EAMv1 and STOCH, respectively. The large-scale precipitation shows very similar contribution distributions in the two simulations, except for the largest rain rates which make only a small contribution to the total. For the most part, large-scale precipitation is not affected by how convection is treated in the model, with both simulations having a maximum contribution near 22 mm d^{-1}. On the other hand, the convective contribution is very different between the two simulations. Similar to the total precipitation, the peak contribution to convective precipitation is at a much smaller rainfall rate in EAMv1 than in STOCH.

Besides precipitation frequency and intensity, another important higher order statistic of precipitation is the duration of precipitation events; it measures the intermittency of precipitation (Trenberth et al. 2017). Using 3-hourly data, we calculate the duration of rainfall events as continuous number of hours of precipitation exceeding a threshold value of 1 mm d^{-1}. Figure 7 shows the frequency of precipitation events for different durations over the tropics. 80% of TRMM observed precipitation events lasts for 3 hours or less, 18% lasts for 6 hours and 2% lasts for 9 hours. In contrast, both EAMv1 and STOCH produce very small proportions (~15%) of precipitation events that last for 3 hours or less. The frequency of precipitation events lasting 9 hours or longer is extremely overestimated in the model simulations, with some lasting for as long as 21 hours. This suggests that convection in the model lacks the observed intermittency (Trenberth et al. 2017) and the use of the stochastic convection scheme does not improve this aspect of the simulated convection.

3.3 Sensitivity of rainfall intensity PDF to vertical resolution

A significant modification among several changes in EAMv1 from CAM5 is a much finer vertical resolution, increasing from 30 levels in CAM5 to 72 levels in EAMv1. Within the PBL alone EAMv1 has 17 layers compared to 5 layers in CAM5, and the thickness of approximately 20 m for the lowest model layer in EAMv1 is much thinner than that in CAM5, which is 100 m (Xie et al., 2018). The increased resolution in the PBL in EAMv1 will likely affect the convection behavior through PBL-convection interactions. In Fig. 3 we showed that the precipitation intensity pdf is significantly improved with the introduction of the stochastic convection scheme. However, the improvement was not as striking as that shown in Wang et al. (2016) for CAM5. We suspect that this is primarily due to the enhanced vertical resolution in EAMv1 rather than other changes in model physics parameterizations, tunings, or the model dynamic core. To confirm this, EAMv1-30L and STOCH-30L runs with a vertical resolution of 30 layers are conducted and compared with the EAMv1 and STOCH runs with the default 72 vertical layers. As seen in Figure 8, when switching to a configuration of 30 vertical layers, the performance of the STOCH-30L run is very similar to that in CAM5 (Wang et al., 2016). The frequency distribution of rainfall intensity between 60 and 140 mm d^{-1} almost falls on top of that in TRMM. The PDF of rain intensity in the EAMv1-30L run is also closer to TRMM observations compared to the EAMv1 run (Fig. 8a). For EAMv1, both convective and large-scale precipitation becomes more intense in the 30-level configuration. The resolution-dependence of large-scale precipitation is consistent with the scale analysis in Rauscher et al. (2016). In their Equation (2), if the terms are rearranged to solve for vertical velocity (ω), it gives $\omega \propto \Delta p$, the vertical grid-spacing in pressure coordinates. Stronger vertical velocity would lead to more intense precipitation. In STOCH-30L, while the frequency of more intense convective precipitation is increased, the frequency of more intense large-scale precipitation is decreased, probably affected by the moisture depletion from strong convective precipitation (Fig. 8b&c).

The causes of the sensitivity of convective precipitation to vertical resolution are further examined below. In the ZM convection scheme, the amount of convection is linked to dilute CAPE (for convenience we will simply call it CAPE below with the understanding that it refers to dilute CAPE). Thus, in Figure 9 we present the joint PDF of convective precipitation and CAPE over the tropics in the four simulations. Note that all parameter settings are identical between EAMv1 and EAMv1-30L except the vertical resolution. Both EAMv1 and EAMv1-30L show an approximately linear relationship between CAPE and convective precipitation. The CAPE values are generally smaller in EAMv1-30L than in EAMv1, as can be seen from the frequency of occurrence of both large and medium CAPE values. However, the slope of the maximum occurrence frequency is almost twice as large in EAMv1-30L as in EAMv1 (Fig. 9a&b), giving the higher frequency of larger convective precipitation as seen in Fig. 8. This is because a coarser vertical resolution means stronger vertical mixing, which results in higher precipitation for given CAPE values. For a given precipitation rate that the model produces, there is in general a large range of CAPE values and the CAPE values in EAMv1 are predominantly larger than in EAMv1-30L as can be seen from the pdf distribution in Fig. 9a and b. Compared to EAMv1, the smaller CAPE values in EAMv1-30L are caused by higher parcel launching levels due to thicker model layers near the surface, where the most unstable air is often found (figure not shown). There is also a bifurcation for medium to large CAPE values. This is likely related to atmospheric moisture conditions in the atmosphere: for the same CAPE values there is less precipitation when the atmosphere is dry, and vice versa. With the introduction of the stochastic deep convection scheme, there are no longer approximately linear relations between CAPE and convective precipitation (Fig. 9c&d) in spite of the fact that the CAPE-based closure is still used to determine the cloud base mass flux (the ensemble mean). This is surprising; it implies that for a given convectively unstable atmospheric thermodynamic condition, the use of the stochastic scheme often inhibits the triggering of convection, thereby allowing for the buildup of CAPE for (the less frequently occurring) stronger convection. Similar to EAMv1, smaller (larger) CAPE values occur more (less) frequently in STOCH-30L due to higher parcel launching levels. Also, the small and moderate values of CAPE have larger probabilities to precipitate more in STOCH-30L compared to STOCH.

Over the ARM SGP and GOAmazon sites, no linear relationship is seen between the total precipitation and CAPE in observations (Fig. 10). At the SGP site, high CAPE values generally correspond to low precipitation. At the GOAmazon site, high precipitation values correspond to medium values of CAPE, somewhat resembling the STOCH simulation, although the observed CAPE values at the GOAmazon site are much smaller than those in the simulations.

3.4 Mean state

So far, we have shown that the introduction of a stochastic convection scheme into the E3SM atmospheric model can significantly improve the simulation of short-term variability and intensity pdf of precipitation. In climate model development efforts, it is important that an improvement in some aspects of the model does not lead to degradation of other aspects, at least not to outweigh the improvement. Thus, it is imperative that we examine the climate mean fields as well. Fig. 11 shows the global distribution of annual mean precipitation in GPCP observations and simulations, as well as the differences of total, convective, and large-scale precipitation between the STOCH and EAMv1 runs. Overall, the geographical distributions of precipitation in the two simulations are similar to those in observations, but both overestimate the tropical precipitation (Fig. 11a-c). There is a slight increase of rainfall over the tropical western Pacific, equatorial Indian Ocean and Africa and a slight decrease over India and Amazonia in the STOCH simulation (Fig. 11d). Most of these changes are from convective precipitation except over equatorial Africa where the changes are from large-scale precipitation (Fig. 11e&f).

The zonal mean of temperature and specific humidity from ERAI and the model biases are shown in Figure 12. For temperature, EAMv1 produces mostly negative biases in the entire troposphere over the tropics and subtropics and positive biases in the lower troposphere in high latitudes. With the stochastic deep convection scheme used, the temperature changes in STOCH are very minor, increasing slightly from EAMv1. In the simulation of specific humidity, there are positive biases in the lower troposphere across all latitudes and negative biases above 900 hPa over the tropics and subtropics in EAMv1. In comparison with EAMv1, the negative biases are alleviated but the positive biases are increased slightly in STOCH.

The overall difference in model performance as measured by the commonly used mean climate metrics between EAMv1 and STOCH runs is summarized in the Taylor diagram (Fig. 13). Most metrics are comparable between the two simulations except precipitation, especially over land where STOCH shows a larger standard deviation than both GPCP and EAMv1. In short, the mean climate does not change much after the incorporation of the stochastic convection scheme in EAMv1. This is practically desirable since one does not need to heavily retune the model, a task that is often time-consuming and more of engineering than scientific interest.

3.5. Response to climate warming

Another aspect of interest concerns the model's response to climate change. It is well known that the estimated climate sensitivity for future climate projections is sensitive to changes in model physics parameterizations (Golaz et al. 2019). With the stochastic deep convection parameterization, it is necessary to check if the response of precipitation and associated extremes to climate warming differs. As seen in Fig. 14, relative to the current climate simulations, the geographical patterns and magnitudes of annual mean precipitation changes normalized by the global-mean surface air warming (ΔT_{sa}) in the +4K SST warming simulations (i.e., $(P_{+4k} - P)/P/\Delta T_{sa}$, units: %/K) with and without the stochastic deep convection scheme are very similar, both showing maximum increases over the ITCZ, the western Pacific and the Indian Ocean. Pendergrass et al., (2019) found that the response of extreme precipitation to warming follows a nonlinear relation:

$$\frac{dr_x}{dT_{sa}} = aT_{sa} \quad (11)$$

or

$$r_x = \frac{1}{2}aT_{sa}^2 + b \quad (12)$$

where r_x is a rainfall extreme index (here using R95p, the total rainfall from the days with daily rainfall intensity exceeding 95th percentile of the daily precipitation distribution), T_{sa} is the global-mean surface air temperature in a warmer world, and a is the slope of dr_x/dT_{sa} versus T_{sa} measuring the strength of the nonlinear response of extreme rainfall to warming. At each grid point, $dr_x \approx \Delta r_x$ is equal to R95p in a warmer world minus that under the current climate and normalized by the global-mean surface air warming ($dT_{sa} \approx \Delta T_{sa}$). With T_{sa} in the +4K SSTs warming simulations and the calculated dr_x/dT_{sa}, the global distributions of the slope, a (units: %/K^2), with and without the stochastic deep convection scheme are displayed in Fig. 14c&d. Although the stochastic deep convection parameterization introduces stochasticity into convection and significantly improves the underestimated frequency of intense precipitation under the current climate (Wang et al., 2017), it does not lead to a different nonlinear response of precipitation extremes in a warmer world. The resemblance of the coefficient a between the two simulations results from the similar response of the fractional change in r_x to global warming

(Fig. 14e&f). Increasing circulation strength as the climate warms is considered to be the main driver for the nonlinear relationship between tropical precipitation extremes and global-mean surface air temperature (Pendergrass et al., 2019), and it is possible that the circulation changes with and without the stochastic deep convection scheme are similar. Relative to their respective current climate states, the responses of the EAMv1-4K and STOCH-4K runs show similar geographical distributions with comparable maximum nonlinearity over the tropical Pacific and Atlantic and the Indian Ocean which bears some resemblance to that in Pendergrass et al. (2019).

4. Summary

In this study, we implemented the stochastic deep convection scheme (Plant and Craig, 2008; Wang et al., 2016) into the DOE EAMv1 and investigated its impact on the simulation of precipitation. Several improvements are observed with the use of the stochastic convection scheme: (1) the weak intraseasonal and synoptic-scale variabilities in EAMv1 are enhanced to levels much closer to those in observations; (2) the “too much light rain and too little heavy rain” bias over the tropics is significantly alleviated due to less frequent occurrence of drizzling convection and more frequent occurrence of intense large-scale and convective precipitation contributing to enhanced heavy rain; (3) the simulated peak precipitation rates (the amount mode) in the precipitation amount distribution, which contribute the most to the total amount of precipitation, are larger and are in better agreement with those in TRMM and GPCP observations.

While the improvement in the simulated PDF of rainfall intensity is significant, it is less than what we had expected based on our earlier work with the NCAR CAM5 (Wang et al., 2016). Since there are many changes from CAM5 to EAMv1, including vertical resolution, model dynamic core and physics parameterizations, it is not clear which changes are related to the difference in the improvement of the simulated rainfall pdf. Two sensitivity tests were performed to elucidate this, both with a coarser vertical resolution configuration of 30 layers (i.e., EAMv1-30L and SOTC-30L) as in CAM5. The STOCH-30L run successfully reproduces the frequency distribution of rainfall intensity found by Wang et al. (2016) with an increased frequency of convective precipitation intensities between 60 and 140 mm d^{-1}. This increase is explained by the fact that small and moderate values of CAPE generate more convective precipitation from the altered relation between them compared to the 72-level configuration due to fewer model layers in the 30-level resolution. Since vertical velocity in general increases with the vertical grid spacing, the increase of large-scale precipitation also contributes to the increased frequency of total precipitation intensities in the 30-level configuration.

For any changes in model physics parameterization that improve some aspects of the model performance, it is important that other aspects are not degraded. It is known in the climate modeling community that improved intraseasonal variability is often accompanied by a degradation of the mean state (e.g., Kim et al. 2011; Klingaman and Demott, 2020). We showed that the mean states in tropospheric temperature, moisture as well as precipitation are not much different with or without the use of the stochastic convection scheme, and neither are the responses of mean precipitation and precipitation extremes to climate warming. This is encouraging and desirable for model development efforts. However, we note that for higher horizontal resolutions (Caldwell et al., 2019) or a regionally refined mesh version of EAMv1 (Tang et al., 2019), spatial averaging of the input fields of the stochastic scheme would be needed to make use of convective quasi-equilibrium over a larger domain. This could be challenging for computational efficiency and it requires further research in the future.

Code and data availability. The E3SMv1 source code can be downloaded from the E3SM official website https://e3sm.org/. The stochastic convection code is accessible from an open repository Zenodo (http://doi.org/10.5281/zenodo.4543261). The GPCP 1DD data is available from NASA GSFC RSD (https://psl.noaa.gov/data/gridded/data.gpcp.html). TRMM and GPM data are available from https://gpm.nasa.gov/data/directory. The availability of daily precipitation observations from the FROGS database is described in Roca et al. (2019). The ARM observations over the SGP and GOAmazon sites are available from https://www.arm.gov/data. The EAMv1 simulation output and a mapping file are provided in Zenodo (http://doi.org/10.5281/zenodo.3902998 and http://doi.org/10.5281/zenodo.4543233).

Author contributions. GJZ conceived the idea. YW developed the model code. YW and WYL conducted the model simulations. YW performed the analysis. YW and GJZ interpreted the results and wrote the paper. All authors participated in the revision and editing of the paper.

Acknowledgements: This work is supported by the National Key Research and Development Program of China Grants 2017YFA0604000, and the National Natural Science Foundation of China Grants 41975126 and 41605074. GJZ is supported by the Department of Energy, Office of

Science, Biological and Environmental Research Program (BER) under Award Number DE-SC0019373. GCC is supported by subproject A1 of the Transregional Collaborative Research Center SFB / TRR 165 "Waves to Weather" (www.wavestoweather.de) funded by the German Research Foundation (DFG). Work at LLNL was performed under the auspices of the U.S. DOE by Lawrence Livermore National Laboratory under contract No. DE-AC52-07NA27344. SX and QT are supported by the DOE Energy Exascale Earth System Model (E3SM) project and HYM is funded by the DOE Regional and Global Model Analysis program area (RGMA) and ASR's Cloud-Associated Parameterizations Testbed (CAPT) project. This research used resources of the National Energy Research Scientific Computing Center, a DOE Office of Science User Facility supported by the Office of Science of the U.S. DOE under Contract No. DE-AC02-05CH11231. The authors would like to thank the two anonymous reviewers for their constructive and helpful comments.

References

Adler, R. F., Huffman, G. J., Chang, A., Ferraro, R., Xie, P.-P., Janowiak, J., Rudolf, B., Schneider, U., Curtis, S., and Bolvin, D.: The version-2 global precipitation climatology project (GPCP) monthly precipitation analysis (1979–present), Journal of hydrometeorology, 4, 1147-1167, 2003.

Bentamy, A., Queffeulou, P., Quilfen, Y., and Katsaros, K.: Ocean surface wind fields estimated from satellite active and passive microwave instruments, IEEE transactions on geoscience and remote sensing, 37, 2469-2486, 1999.

Caldwell, P. M., Mametjanov, A., Tang, Q., Van Roekel, L. P., Golaz, J.-C., Lin, W., Bader, D. C., Keen, N. D., Feng, Y., Jacob, R., Maltrud, M. E., Roberts, A. F., Taylor, M. A., Veneziani, M., Wang, H., Wolfe, J. D., Balaguru, K., Cameron-Smith, P., Dong, L., Klein, S. A., Leung, L. R., Li, H.-Y., Li, Q., Liu, X., Neale, R. B., Pinheiro, M., Qian, Y., Ullrich, P. A., Xie, S., Yang, Y., Zhang, Y., Zhang, K., and Zhou, T.: The DOE E3SM Coupled Model Version 1: Description and Results at High Resolution, Journal of Advances in Modeling Earth Systems, 11, 4095-4146, 10.1029/2019ms001870, 2019.

Cohen, B. G., and Craig, G. C.: Fluctuations in an Equilibrium Convective Ensemble. Part II: Numerical Experiments, Journal of the Atmospheric Sciences, 63, 2005-2015, 10.1175/JAS3710.1, 2006.

Craig, G. C., and Cohen, B. G.: Fluctuations in an Equilibrium Convective Ensemble. Part I: Theoretical Formulation, Journal of the Atmospheric Sciences, 63, 1996-2004, 10.1175/JAS3709.1, 2006.

Dai, A.: Precipitation Characteristics in Eighteen Coupled Climate Models, Journal of Climate, 19, 4605-4630, 10.1175/JCLI3884.1, 2006.

Davies, L., Jakob, C., May, P., Kumar, V. V., and Xie, S.: Relationships between the large-scale atmosphere and the small-scale convective state for Darwin, Australia, Journal of Geophysical Research: Atmospheres, 118, 11,534-511,545, 10.1002/jgrd.50645, 2013.

Gettelman, A., Morrison, H., Santos, S., Bogenschutz, P., and Caldwell, P.: Advanced two-moment bulk microphysics for global models. Part II: Global model solutions and aerosol–cloud interactions, Journal of Climate, 28, 1288-1307, 2015.

Golaz, J.-C., Larson, V. E., and Cotton, W. R.: A PDF-based model for boundary layer clouds. Part I: Method and model description, Journal of the atmospheric sciences, 59, 3540-3551, 2002.

Golaz, J.-C., Caldwell, P. M., Van Roekel, L. P., Petersen, M. R., Tang, Q., Wolfe, J. D., Abeshu, G., Anantharaj, V., Asay-Davis, X. S., Bader, D. C., Baldwin, S. A., Bisht, G., Bogenschutz, P. A., Branstetter, M., Brunke, M. A., Brus, S. R., Burrows, S. M., Cameron-Smith, P. J., Donahue, A. S., Deakin, M., Easter, R. C., Evans, K. J., Feng, Y., Flanner, M., Foucar, J. G., Fyke, J. G., Griffin, B. M., Hannay, C., Harrop, B. E., Hoffman, M. J., Hunke, E. C., Jacob, R. L., Jacobsen, D. W., Jeffery, N., Jones, P. W., Keen, N. D., Klein, S. A., Larson, V. E., Leung, L. R., Li, H.-Y., Lin, W., Lipscomb, W. H., Ma, P.-L., Mahajan, S., Maltrud, M. E., Mametjanov, A., McClean, J. L., McCoy, R. B., Neale, R. B., Price, S. F., Qian, Y., Rasch, P. J., Reeves Eyre, J. E. J., Riley, W. J., Ringler, T. D., Roberts, A. F., Roesler, E. L., Salinger, A. G., Shaheen, Z., Shi, X., Singh, B., Tang, J., Taylor, M. A., Thornton, P. E., Turner, A. K., Veneziani, M., Wan, H., Wang, H., Wang, S., Williams, D. N., Wolfram, P. J., Worley, P. H., Xie, S., Yang, Y., Yoon, J.-H., Zelinka, M. D., Zender, C. S., Zeng, X., Zhang, C., Zhang, K., Zhang, Y., Zheng, X., Zhou, T., and Zhu, Q.: The DOE E3SM Coupled Model Version 1: Overview and Evaluation at Standard Resolution, Journal of Advances in Modeling Earth Systems, 11, 2089-2129, 10.1029/2018ms001603, 2019.

Goswami, B., Khouider, B., Phani, R., Mukhopadhyay, P., and Majda, A.: Improving synoptic and intraseasonal variability in CFSv2 via stochastic representation of organized convection, Geophysical Research Letters, 44, 1104-1113, 2017.

Groenemeijer, P., and Craig, G. C.: Ensemble forecasting with a stochastic convective parametrization based on equilibrium statistics, Atmos. Chem. Phys., 12, 4555-4565, 10.5194/acp-12-4555-2012, 2012.

Hsu, J., and Prather, M. J.: Stratospheric variability and tropospheric ozone, Journal of Geophysical Research: Atmospheres, 114, 2009.

Huffman, G. J., Adler, R. F., Morrissey, M. M., Bolvin, D. T., Curtis, S., Joyce, R., McGavock, B., and Susskind, J.: Global precipitation at one-degree daily resolution from multisatellite observations, Journal of hydrometeorology, 2, 36-50, 2001.

Huffman, G. J., Bolvin, D. T., Nelkin, E. J., Wolff, D. B., Adler, R. F., Gu, G., Hong, Y., Bowman, K. P., and Stocker, E. F.: The TRMM multisatellite precipitation analysis (TMPA): Quasi-global, multiyear, combined-sensor precipitation estimates at fine scales, Journal of hydrometeorology, 8, 38-55, 2007.

Huffman, G., Bolvin, D., and Adler, R.: GPCP version 1.2 1-degree daily (1DD) precipitation data set, World Data Center A, National Climatic Data Center, Asheville, NC [Available at ftp://rsd. gsfc. nasa. gov/pub/1dd-v1. 2/.], 2012.

Huffman, G. J., Bolvin, D. T., and Nelkin, E. J.: Integrated Multi- satellitE Retrievals for GPM (IMERG) technical documentation, available at: https://pmm.nasa.gov/sites/default/files/document_ files/IMERG_doc.pdf (last access: 8 July 2019), 2017.

Jones, T. R., and Randall, D. A.: Quantifying the limits of convective parameterizations, Journal of Geophysical Research: Atmospheres, 116, 10.1029/2010jd014913, 2011.

Kain, J. S., and Fritsch, J. M.: A One-Dimensional Entraining/Detraining Plume Model and Its Application in Convective Parameterization, Journal of the Atmospheric Sciences, 47, 2784-2802, 10.1175/1520-0469(1990)047<2784:AODEPM>2.0.CO;2, 1990.

Kain, J. S.: The Kain–Fritsch Convective Parameterization: An Update, Journal of Applied Meteorology, 43, 170-181, 10.1175/1520-0450(2004)043<0170:TKCPAU>2.0.CO;2, 2004.

Keane, R. J., Craig, G. C., Keil, C., and Zängl, G.: The Plant–Craig Stochastic Convection Scheme in ICON and Its Scale Adaptivity, Journal of the Atmospheric Sciences, 71, 3404-3415, 10.1175/JAS-D-13-0331.1, 2014.

Keane, R. J., Plant, R. S., and Tennant, W. J.: Evaluation of the Plant–Craig stochastic convection scheme (v2. 0) in the ensemble forecasting system MOGREPS-R (24 km) based on the Unified Model (v7. 3), Geoscientific Model Development, 9, 1921-1935, 2016.

Khouider, B., Biello, J., and Majda, A. J.: A stochastic multicloud model for tropical convection, 187-216, 2010.

Kim, D., Sobel, A. H., Maloney, E. D., Frierson, D. M., and Kang, I.-S.: A systematic relationship between intraseasonal variability and mean state bias in AGCM simulations, Journal of Climate, 24, 5506-5520, 2011.

Klingaman, N. P., and Demott, C. A.: Mean State Biases and Interannual Variability Affect Perceived Sensitivities of the Madden-Julian Oscillation to Air-Sea Coupling, Journal of Advances in Modeling Earth Systems, 12, e2019MS001799, 10.1029/2019ms001799, 2020.

Kooperman, G. J., Pritchard, M. S., Burt, M. A., Branson, M. D., and Randall, D. A.: Robust effects of cloud superparameterization on simulated daily rainfall intensity statistics across multiple versions of the C ommunity E arth S ystem M odel, Journal of Advances in Modeling Earth Systems, 8, 140-165, 2016.

Kooperman, G. J., Pritchard, M. S., O'Brien, T. A., and Timmermans, B. W.: Rainfall From Resolved Rather Than Parameterized Processes Better Represents the Present‐Day and Climate Change Response of Moderate Rates in the Community Atmosphere Model, Journal of advances in modeling earth systems, 10, 971-988, 2018.

Larson, V. E., and Golaz, J.-C.: Using probability density functions to derive consistent closure relationships among higher-order moments, Monthly Weather Review, 133, 1023-1042, 2005.

Lin, J. W. B., and Neelin, J. D.: Influence of a stochastic moist convective parameterization on tropical climate variability, Geophysical research letters, 27, 3691-3694, 2000.

Lin, J. W.-B., and Neelin, J. D.: Considerations for stochastic convective parameterization, Journal of the atmospheric sciences, 59, 959-975, 2002.

Liu, X., Ma, P.-L., Wang, H., Tilmes, S., Singh, B., Easter, R., Ghan, S., and Rasch, P.: Description and evaluation of a new four-mode version of the Modal Aerosol Module (MAM4) within version 5.3 of the Community Atmosphere Model, Geoscientific Model Development (Online), 9, 2016.

Loeb, N. G., Wielicki, B. A., Doelling, D. R., Smith, G. L., Keyes, D. F., Kato, S., Manalo-Smith, N., and Wong, T.: Toward optimal closure of the Earth's top-of-atmosphere radiation budget, Journal of Climate, 22, 748-766, 2009.

Martin, S. T., Artaxo, P., Machado, L. A. T., Manzi, A. O., Souza, R. A. F., Schumacher, C., Wang, J., Andreae, M. O., Barbosa, H. M. J., Fan, J., Fisch, G., Goldstein, A. H., Guenther, A., Jimenez, J. L., Pöschl, U., Silva Dias, M. A., Smith, J. N., and Wendisch, M.: Introduction: Observations and Modeling of the Green Ocean Amazon (GoAmazon2014/5), Atmos. Chem. Phys., 16, 4785–4797, https://doi.org/10.5194/acp-16-4785-2016, 2016.

McLinden, C., Olsen, S., Hannegan, B., Wild, O., Prather, M., and Sundet, J.: Stratospheric ozone in 3‐D models: A simple chemistry and the cross‐tropopause flux, Journal of Geophysical Research: Atmospheres, 105, 14653-14665, 2000.

Morrison, H., and Gettelman, A.: A New Two-Moment Bulk Stratiform Cloud Microphysics Scheme in the Community Atmosphere Model, Version 3 (CAM3). Part I: Description and Numerical Tests, Journal of Climate, 21, 3642-3659, 10.1175/2008JCLI2105.1, 2008.

O’Gorman, P. A., and Schneider, T.: The physical basis for increases in precipitation extremes in simulations of 21st-century climate change, Proceedings of the National Academy of Sciences of the United States of America, 106, 14773-14777, 2009.

Palmer, T. N.: A nonlinear dynamical perspective on model error: A proposal for non-local stochastic-dynamic parametrization in weather and climate prediction models, Quarterly Journal of the Royal Meteorological Society, 127, 279-304, 2001.

Palmer, T. N.: Towards the probabilistic Earth-system simulator: a vision for the future of climate and weather prediction†, Quarterly Journal of the Royal Meteorological Society, 138, 841-861, 2012.

Pendergrass, A., Coleman, D., Deser, C., Lehner, F., Rosenbloom, N., and Simpson, I.: Nonlinear response of extreme precipitation to warming in CESM1, Geophysical Research Letters, 46, 10551-10560, 2019.

Peters, K., Jakob, C., Davies, L., Khouider, B., and Majda, A. J.: Stochastic Behavior of Tropical Convection in Observations and a Multicloud Model, Journal of the Atmospheric Sciences, 70, 3556-3575, 2013.

Peters, K., Crueger, T., Jakob, C., and Mobis, B.: Improved MJO-simulation in ECHAM6.3 by coupling a Stochastic Multicloud Model to the convection scheme, Journal of Advances in Modeling Earth Systems, 9, 193-219, 2017.

Plant, R. S., and Craig, G. C.: A Stochastic Parameterization for Deep Convection Based on Equilibrium Statistics, Journal of the Atmospheric Sciences, 65, 87-105, 10.1175/2007JAS2263.1, 2008.

Rasch, P., Xie, S., Ma, P. L., Lin, W., Wang, H., Tang, Q., Burrows, S., Caldwell, P., Zhang, K., and Easter, R.: An overview of the atmospheric component of the Energy Exascale Earth System Model, Journal of Advances in Modeling Earth Systems, 11, 2377-2411, 2019.

Rauscher, S. A., O'Brien, T. A., Piani, C., Coppola, E., Giorgi, F., Collins, W. D., and Lawston, P. M.: A multimodel intercomparison of resolution effects on precipitation: simulations and theory, Clim Dyn, 47, 2205-2218, 10.1007/s00382-015-2959-5, 2016.

Roca, R.: Estimation of extreme daily precipitation thermodynamic scaling using gridded satellite precipitation products over tropical land, Environmental Research Letters, 14, 095009, 10.1088/1748-9326/ab35c6, 2019.

Roca, R., Alexander, L. V., Potter, G., Bador, M., Jucá, R., Contractor, S., Bosilovich, M. G., and Cloché, S.: FROGS: a daily 1° × 1° gridded precipitation database of rain gauge, satellite and reanalysis products, Earth Syst. Sci. Data, 11, 1017-1035, 10.5194/essd-11-1017-2019, 2019.

Sakradzija, M., Seifert, A., and Heus, T.: Fluctuations in a quasi-stationary shallow cumulus cloud ensemble, Nonlin. Processes Geophys., 22, 65-85, 10.5194/npg-22-65-2015, 2015.

Simmons, A., Uppala, S., Dee, D., and Kobayashi, S.: ERA-Interim: New ECMWF reanalysis products from 1989 onwards, ECMWF Newsl., 110, 1–11, 2007.

Stone, D., Risser, M. D., Angelil, O., Wehner, M., Cholia, S., Keen, N., Krishnan, H., Obrien, T. A., and Collins, W. D.: A basis set for exploration of sensitivity to prescribed ocean conditions for estimating human contributions to extreme weather in CAM5.1-1degree, Weather and climate extremes, 19, 10-19, 2018.

Tang, S., Xie, S., Zhang, Y., Zhang, M., Schumacher, C., Upton, H., Jensen, M. P., Johnson, K. L., Wang, M., Ahlgrimm, M., Feng, Z., Minnis, P., and Thieman, M.: Large-scale vertical velocity, diabatic heating and drying profiles associated with seasonal and diurnal variations of convective systems observed in the GoAmazon2014/5 experiment, Atmos. Chem. Phys., 16, 14249–14264, https://doi.org/10.5194/acp-16-14249-2016, 2016.

Tang, Q., Klein, S. A., Xie, S., Lin, W., Golaz, J.-C., Roesler, E. L., Taylor, M. A., Rasch, P. J., Bader, D. C., and Berg, L. K.: Regionally refined test bed in E3SM atmosphere model version 1 (EAMv1) and applications for high-resolution modeling, Geosci. Model Dev., 12, 2679–2706, https://doi.org/10.5194/gmd-12-2679-2019, 2019.

Trenberth, K. E., Zhang, Y., and Gehne, M.: Intermittency in Precipitation: Duration, Frequency, Intensity, and Amounts Using Hourly Data, Journal of Hydrometeorology, 18, 1393-1412, 10.1175/jhm-d-16-0263.1, 2017.

Wang, Y., Liu, X., Hoose, C., and Wang, B.: Different contact angle distributions for heterogeneous ice nucleation in the Community Atmospheric Model version 5, Atmospheric Chemistry and Physics, 10411, 2014.

Wang, Y., and Zhang, G. J.: Global climate impacts of stochastic deep convection parameterization in the NCAR CAM5, Journal of Advances in Modeling Earth Systems, 8, 1641-1656, doi:10.1002/2016MS000756, 2016.

Wang, Y., Zhang, G. J., and Craig, G. C.: Stochastic convective parameterization improving the simulation of tropical precipitation variability in the NCAR CAM5, Geophysical Research Letters, 43, 6612-6619, doi:10.1002/2016GL069818, 2016.

Wang, Y., Zhang, G. J., and Jiang, Y.: Linking Stochasticity of Convection to Large-Scale Vertical Velocity to Improve Indian Summer Monsoon Simulation in the NCAR CAM5, Journal of Climate, 31, 6985-7002, 10.1175/jcli-d-17-0785.1, 2018.

Wang, Y., W. Xia, X. Liu, S. Xie, W. Lin, Q. Tang, H.-Y. Ma, Y. Jiang, B. Wang, and G. J. Zhang: Disproportionate control on aerosol burden by light rain, *Nature Geoscience*, https://doi.org/10.1038/s41561-020-00675-z, 2021.

Watson, P. A. G., Berner, J., Corti, S., Davini, P., Von Hardenberg, J., Sanchez, C., Weisheimer, A., and Palmer, T. N.: The impact of stochastic physics on tropical rainfall variability in global climate models on daily to weekly time scales, Journal of Geophysical Research, 122, 5738-5762, 2017.

Webb, M. J., Andrews, T., Bodas-Salcedo, A., Bony, S., Bretherton, C. S., Chadwick, R., Chepfer, H., Douville, H., Good, P., and Kay, J. E.: The cloud feedback model intercomparison project (CFMIP) contribution to CMIP6, Geoscientific Model Development, 2017, 359-384, 2017.

Willmott, C. J., and Matsuura, K.: Smart interpolation of annually averaged air temperature in the United States, Journal of Applied Meteorology, 34, 2577-2586, 1995.

Xie, P., and Arkin, P. A.: Analyses of Global Monthly Precipitation Using Gauge Observations, Satellite Estimates, and Numerical Model Predictions, Journal of Climate, 9, 840-858, 10.1175/1520-0442(1996)009<0840:AOGMPU>2.0.CO;2, 1996.

Xie, S., R. T. Cederwall, and M. H. Zhang: Developing long-term single-column model/cloud system-resolving model forcing using numerical weather prediction products constrained by surface and top of the atmosphere observations. *J. Geophys. Res., 109*, D01104, doi:10.1029/2003JD004045, 2004.

Xie, S., Lin, W., Rasch, P. J., Ma, P. L., Neale, R., Larson, V. E., Qian, Y., Bogenschutz, P. A., Caldwell, P., and Cameron‐Smith, P.: Understanding cloud and convective characteristics in version 1 of the E3SM atmosphere model, Journal of Advances in Modeling Earth Systems, 10, 2618-2644, 2018.

Xie, S., Wang, Y., Lin, W., Ma, H., Tang, Q., Tang, S., Zheng, X., Golaz, J., Zhang, G. J., and Zhang, M.: Improved Diurnal Cycle of Precipitation in E3SM With a Revised Convective Triggering Function, Journal of Advances in Modeling Earth Systems, 11, 2290-2310, 2019.

Zhang, G. J., and Mu, M.: Simulation of the Madden–Julian Oscillation in the NCAR CCM3 Using a Revised Zhang–McFarlane Convection Parameterization Scheme, Journal of Climate, 18, 4046-4064, 2005a.

Zhang, G. J., and Mu, M.: Effects of modifications to the Zhang-McFarlane convection parameterization on the simulation of the tropical precipitation in the National Center for Atmospheric Research Community Climate Model, version 3, Journal of Geophysical Research: Atmospheres, 110, D09109, 10.1029/2004JD005617, 2005b.

Zhang, G. J., Song, X., and Wang, Y.: The double ITCZ syndrome in GCMs: A coupled feedback problem among convection, clouds, atmospheric and ocean circulations, Atmospheric Research, 2019.

Zhang, G. J., and Wang, H.: Toward mitigating the double ITCZ problem in NCAR CCSM3, Geophysical Research Letters, 33, 2006.

Zhang, Y., Xie, S., Lin, W., Klein, S. A., Zelinka, M., Ma, P. L., Rasch, P. J., Qian, Y., Tang, Q., and Ma, H. Y.: Evaluation of clouds in version 1 of the E3SM atmosphere model with satellite simulators, Journal of Advances in Modeling Earth Systems, 11, 1253-1268, 2019.

Table captions:

Table 1. List of simulations.

Simulation	Years	Vertical Levels	Description
EAMv1	6	72	Standard EAMv1 with the default deterministic ZM deep convection scheme for simulating the current climate[1]
STOCH	6	72	Same as EAMv1, but coupling with the PC stochastic deep convection scheme with the deterministic ZM deep convection scheme
EAMv1-30L	6	30	Same as EAMv1, but using a vertical resolution configuration of 30 layers
STOCH-30L	6	30	Same as STOCH, but using a vertical resolution configuration of 30 layers
EAMv1-4K	3	72	Same as EAMv1, but for simulating a warmer world[2]
STOCH-4K	3	72	Same as STOCH, but for simulating a warmer world

[1]Atmosphere-only simulations, using fully prognostic atmosphere and land models with prescribed, seasonally varying climatological present-day sea surface temperatures (SSTs) and sea ice extent, recycled yearly.

[2]For simulating a warmer world, the atmosphere-only simulations are subjected to a composite SST warming pattern derived from the Coupled Model Intercomparison Project Phase 3 (CMIP3) coupled models.

Figure captions

Figure 1. Spatial distributions of the 20–80 day variance of rainfall from (a) the Xie-Arkin observations, (b) TRMM, (c) EAMv1, and (d) STOCH, respectively (units: $mm^2\ d^{-2}$).

Figure 2. Spatial distributions of the synoptic variance of rainfall from (a) TRMM, (b) EAMv1, and (c) STOCH, respectively (units: $mm^2\ d^{-2}$).

Figure 3. Frequency distributions of (a) total (solid line), (b) convective (solid line) and large-scale (dashed line) precipitation intensity over the tropics (20^{o}S, 20^{o}N) for EAMv1 (blue) and STOCH (red) respectively. For total precipitation, the TRMM observations (black) and ensemble mean of multiple observations (Obs_ens, purple) where each observation is denoted by the gray line are included for evaluation.

Figure 4. Frequency distributions of total precipitation intensity over Amazon (20^{o}S-5^{o}N, 40^{o}W-80^{o}W), tropical western Pacific (TWP) (0^{o}N-15^{o}N, 130^{o}E-170^{o}E), India (14^{o}N-26.5^{o}N, 74.5^{o}E-94^{o}E; for June-September), Maritime Continent (MC) (10^{o}S-10^{o}N, 90^{o}E-160^{o}E), Southern Great Plains (SGP) (37^{o}N-42^{o}N, 90^{o}W-110^{o}W; for May-August) and eastern China (25^{o}N-35^{o}N, 100^{o}E-120^{o}E; for June-August) for TRMM (black), EAMv1 (blue) and STOCH (red) respectively.

Figure 5. Spatial distributions of frequencies of total rainfall intensity larger than (top row) 1 $mm\ d^{-1}$, (middle row) between 1 and 20 $mm\ d^{-1}$ and (bottom row) larger than 20 $mm\ d^{-1}$ for TRMM, EAMv1 and STOCH, respectively.

Figure 6. Annual mean rainfall amount distributions of (a) total precipitation (solid line) over the tropics (20^{o}S, 20^{o}N) for GPCP 1DD (grey), TRMM (black), EAMv1 (blue) and STOCH (red), respectively. Individual distributions of (b) convective (solid line) and large-scale (dashed line) precipitation in EAMv1 (blue) and STOCH (red) are also shown. The rainfall intensity on the x-axis is on a logarithmic scale with bin intervals of $\Delta \ln(R) = \Delta R/R = 0.1$.

Figure 7. Histogram of percentage frequency of total rainy events as a function of their duration using 3-hourly data (conditional probability of rainfall, given rainfall the previous times) from TRMM (black), EAMv1 (blue) and STOCH (red) for the threshold rainfall rate of 1 $mm\ d^{-1}$ over the tropics.

Figure 8. Same as Fig. 3, but including PDFs for EAMv1-30L and STOCH-30L (both dashed lines).

Figure 9. Joint PDFs of CAPE versus convective precipitation over the tropics (20^{o}S, 20^{o}N) from (a) EAMv1, (b) EAMv1-30L, (c) STOCH, and (d) STOCH-30L, respectively.

Figure 10. Scatterplots of total precipitation versus CAPE at the ARM (a-c) SGP and (d-f) Amazon sites for (a & d) observations calculated from multi-year sounding data (2014-2015 for Amazon and 2004-2018 for SGP), (b & e) EAMv1 and (c & f) STOCH.

Figure 11. Global distributions of total precipitation for (a) GPCP, (b) EAMv1, and (c) STOCH, and differences of (d) total, (e) convective and (f) large-scale precipitation between STOCH and EAMv1. Differences with a confidence level greater than 95% in (d-f) are stippled.

Figure 12. Annual and zonal mean cross sections of (a-c) temperature and (d-f) specific humidity for (a & d) ERAI and differences for (b & e) EAMv1-ERAI and (c &f) STOCH-EAMv1. Differences with a confidence level greater than 95% in between STOCH and EAMv1 are stippled.

Figure 13. Taylor diagram with metrics for STOCH, compared with EAMv1.

Figure 14. Geographical distributions of responses of (a & b) annual mean precipitation, (c & d) the coefficient *a*, and (e & f) the fractional change in precipitation extremes (R95p) to climate warming from +4K experiments. Differences with a confidence level greater than 95% are stippled.

Figures

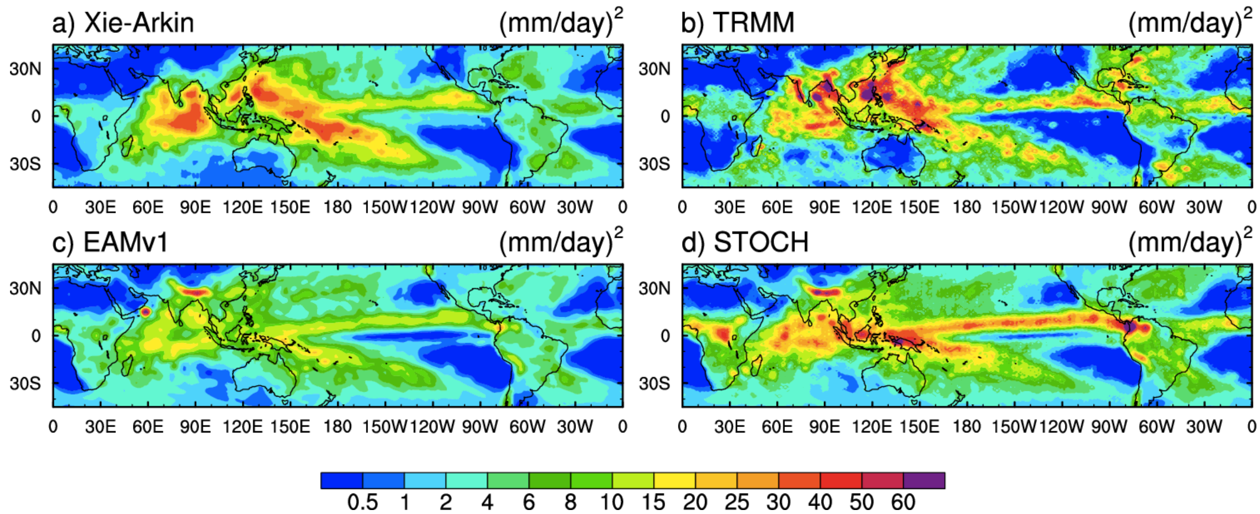

Figure 1. Spatial distributions of the 20–80 day variance of rainfall from (a) the Xie-Arkin observations, (b) TRMM, (c) EAMv1, and (d) STOCH, respectively (units: $mm^2\ d^{-2}$).

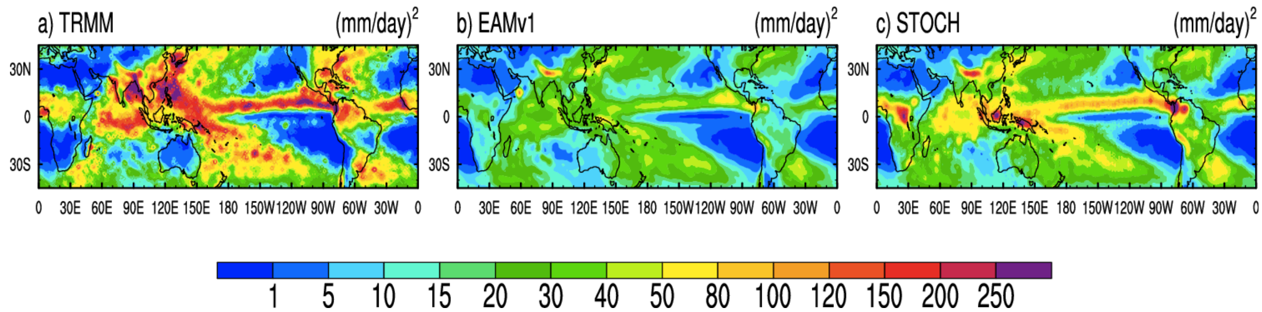

Figure 2. Spatial distributions of the synoptic variance of rainfall from (a) TRMM, (b) EAMv1, and (c) STOCH, respectively (units: mm^2 d^{-2}).

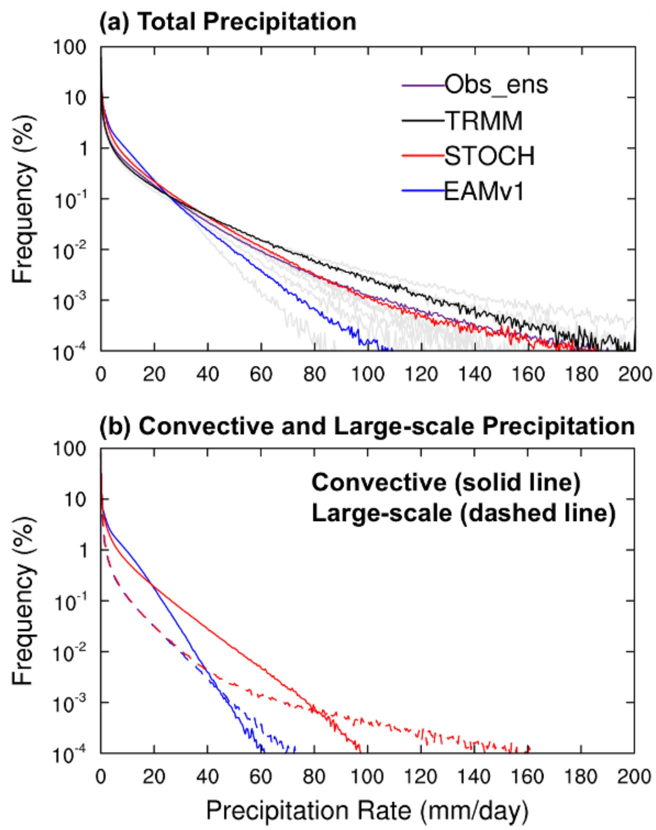

Figure 3. Frequency distributions of (a) total (solid line), (b) convective (solid line) and large-scale (dashed line) precipitation intensity over the tropics (20^{o}S, 20^{o}N) for EAMv1 (blue) and STOCH (red) respectively. For total precipitation, the TRMM observations (black) and ensemble mean of multiple observations (Obs_ens, purple) where each observation is denoted by the gray line are included for evaluation.

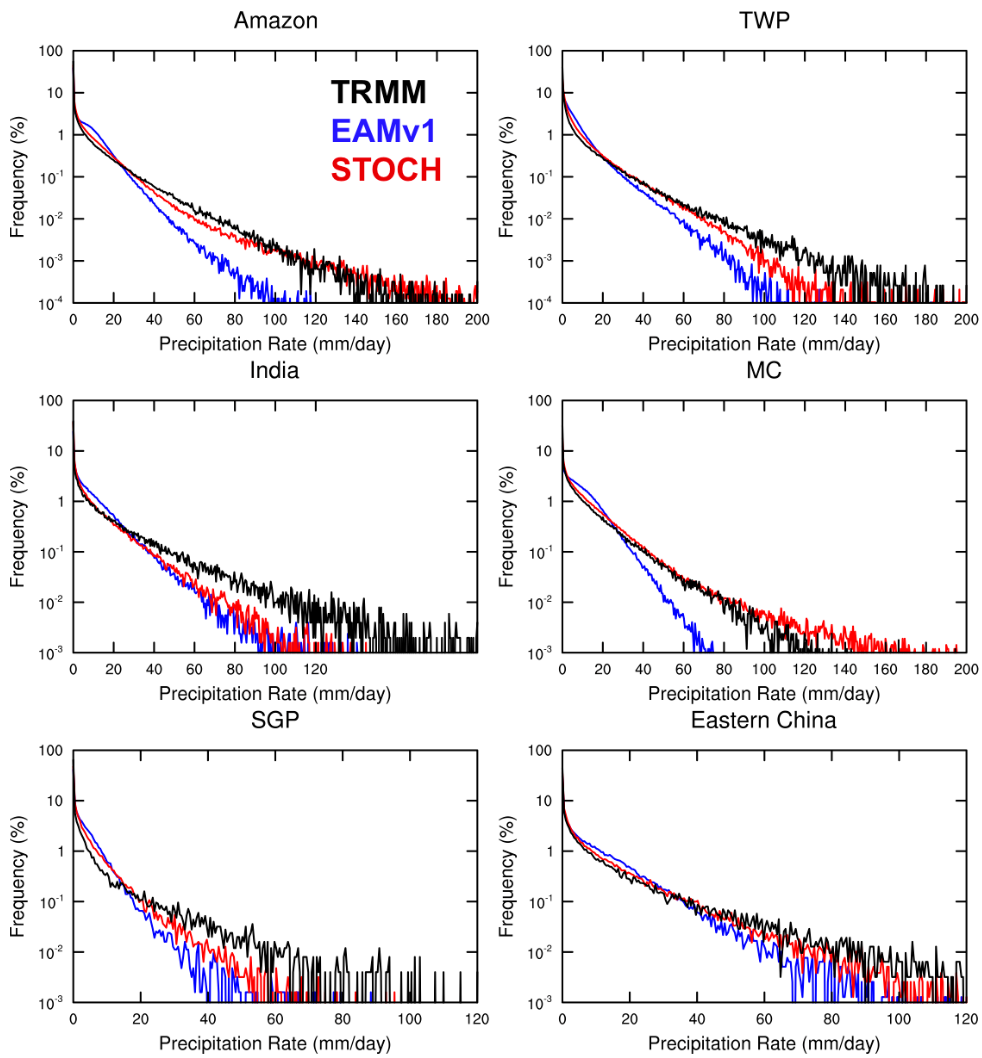

Figure 4. Frequency distributions of total precipitation intensity over Amazon (20^{o}S-5^{o}N, 40^{o}W-80^{o}W), tropical western Pacific (TWP) (0^{o}N-15^{o}N, 130^{o}E-170^{o}E), India (14^{o}N-26.5^{o}N, 74.5^{o}E-94^{o}E; for June-September), Maritime Continent (MC) (10^{o}S-10^{o}N, 90^{o}E-160^{o}E), Southern Great Plains (SGP) (37^{o}N-42^{o}N, 90^{o}W-110^{o}W; for May-August) and eastern China (25^{o}N-35^{o}N, 100^{o}E-120^{o}E; for June-August) for TRMM (black), EAMv1 (blue) and STOCH (red) respectively.

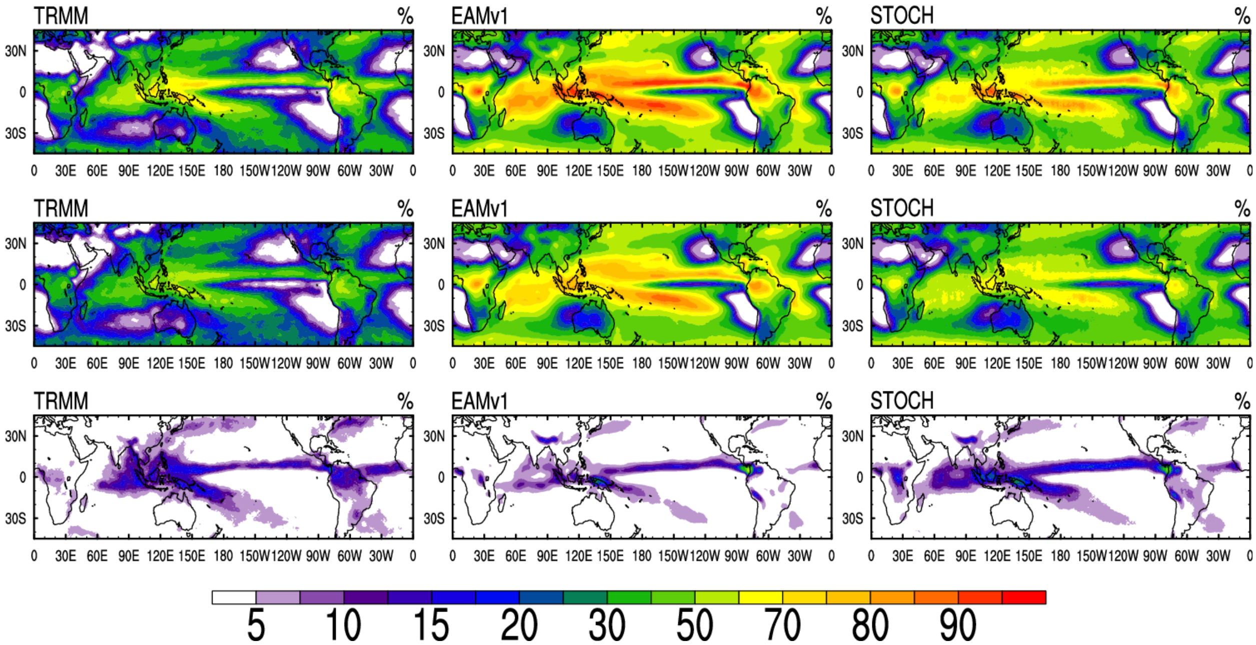

Figure 5. Spatial distributions of frequencies of total rainfall intensity larger than (top row) 1 mm d^{-1}, (middle row) between 1 and 20 mm d^{-1} and (bottom row) larger than 20 mm d^{-1} for TRMM, EAMv1 and STOCH, respectively.

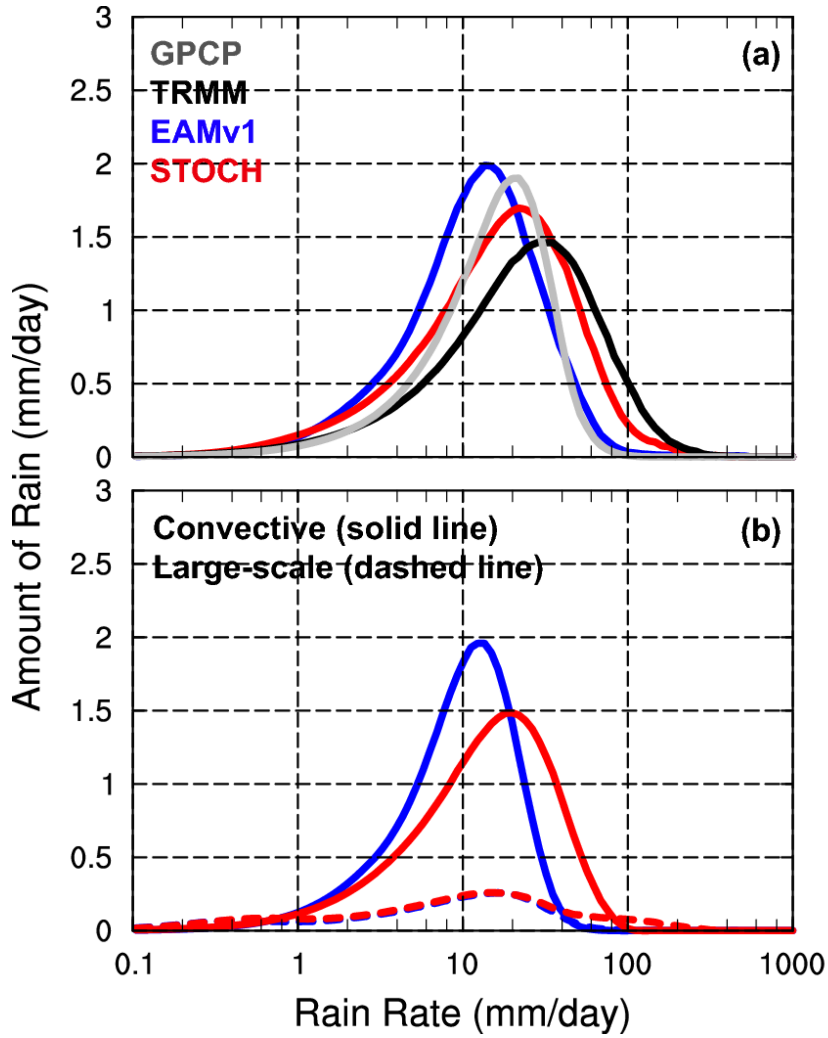

Figure 6. Annual mean rainfall amount distributions of (a) total precipitation (solid line) over the tropics (20^{o}S, 20^{o}N) for GPCP 1DD (grey), TRMM (black), EAMv1 (blue) and STOCH (red), respectively. Individual distributions of (b) convective (solid line) and large-scale (dashed line) precipitation in EAMv1 (blue) and STOCH (red) are also shown. The rainfall intensity on the x-axis is on a logarithmic scale with bin intervals of $\Delta \ln(R) = \Delta R/R = 0.1$.

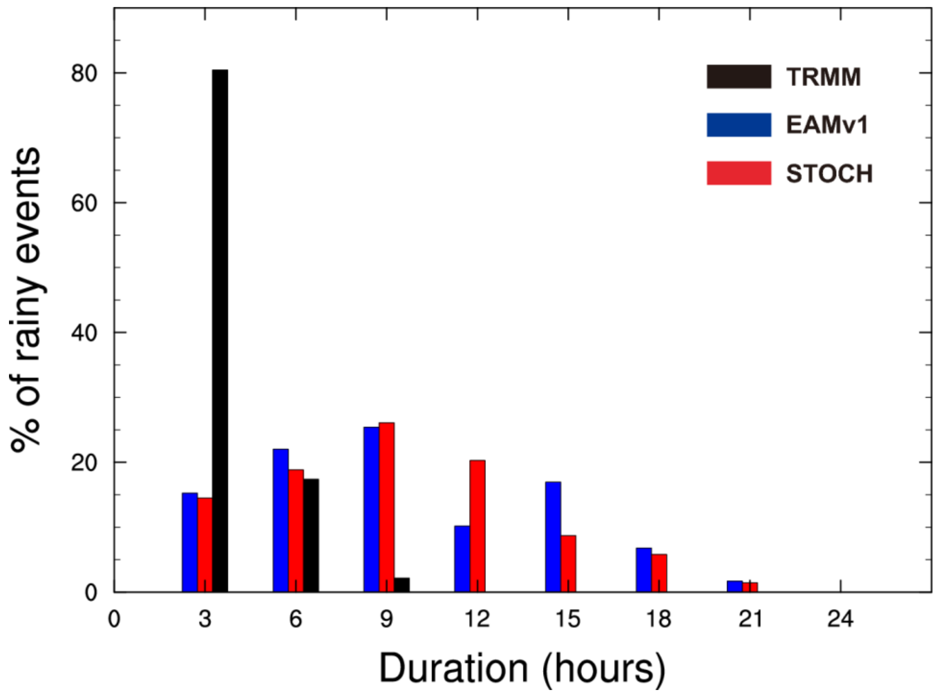

Figure 7. Histograms of percentage frequency of total rainy events as a function of their duration using 3-hourly data (conditional probability of rainfall, given rainfall the previous times) from TRMM (black), EAMv1 (blue) and STOCH (red) for the threshold rainfall rate of 1 mm d^{-1} over the tropics.

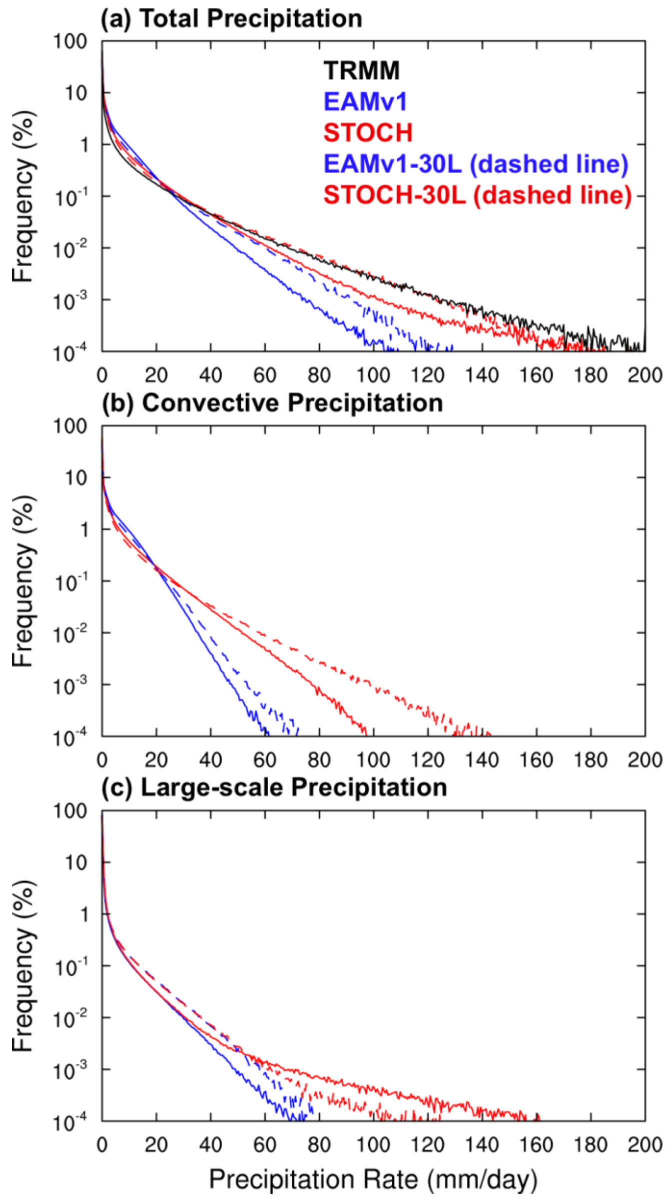

Figure 8. Same as Fig. 3, but including PDFs for EAMv1-30L and STOCH-30L (both dashed lines).

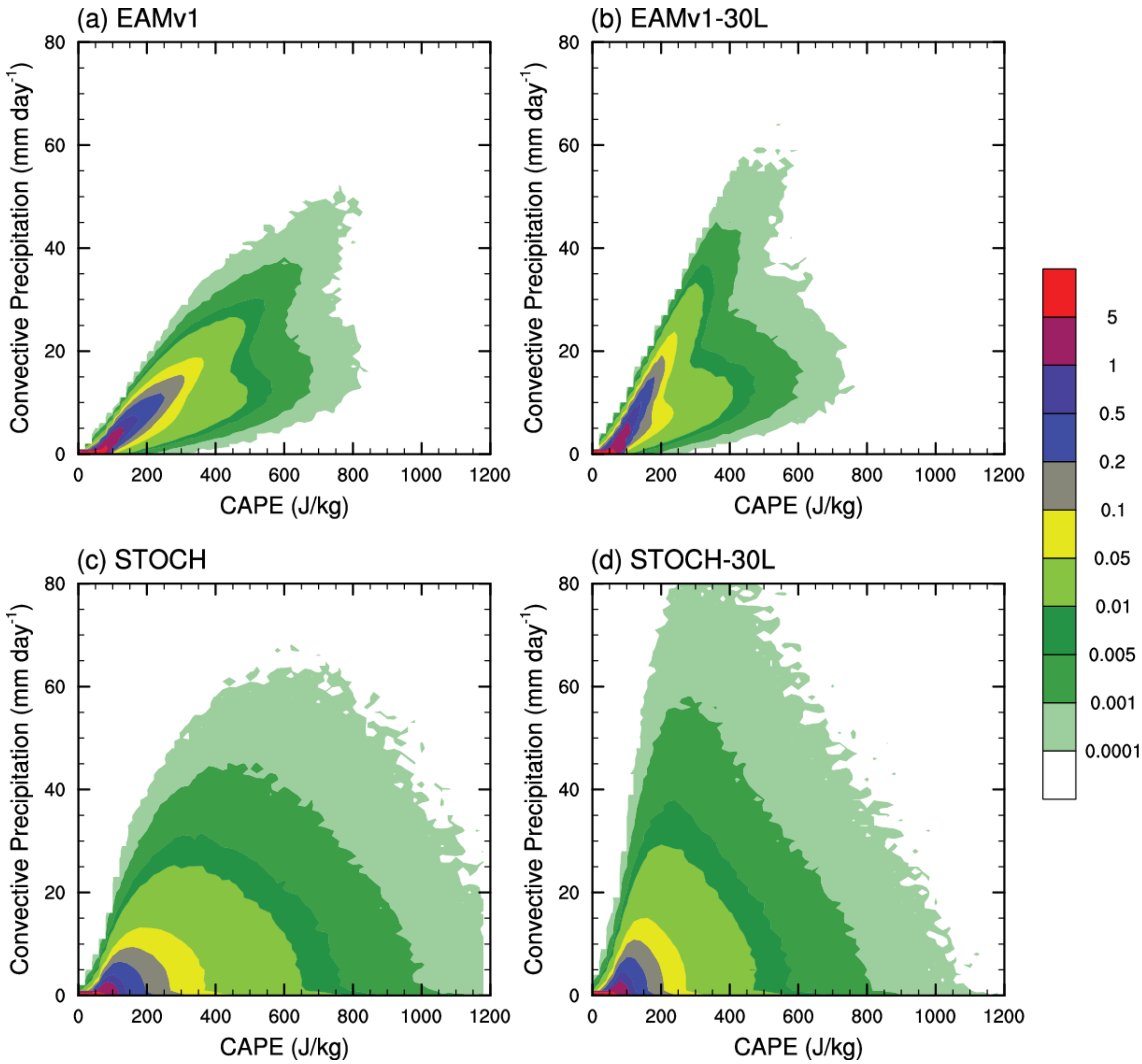

921

922 **Figure 9.** Joint PDFs of CAPE versus convective precipitation over the tropics (20^{o}S, 20^{o}N)

923 from (a) EAMv1, (b) EAMv1-30L, (c) STOCH, and (d) STOCH-30L, respectively.

924

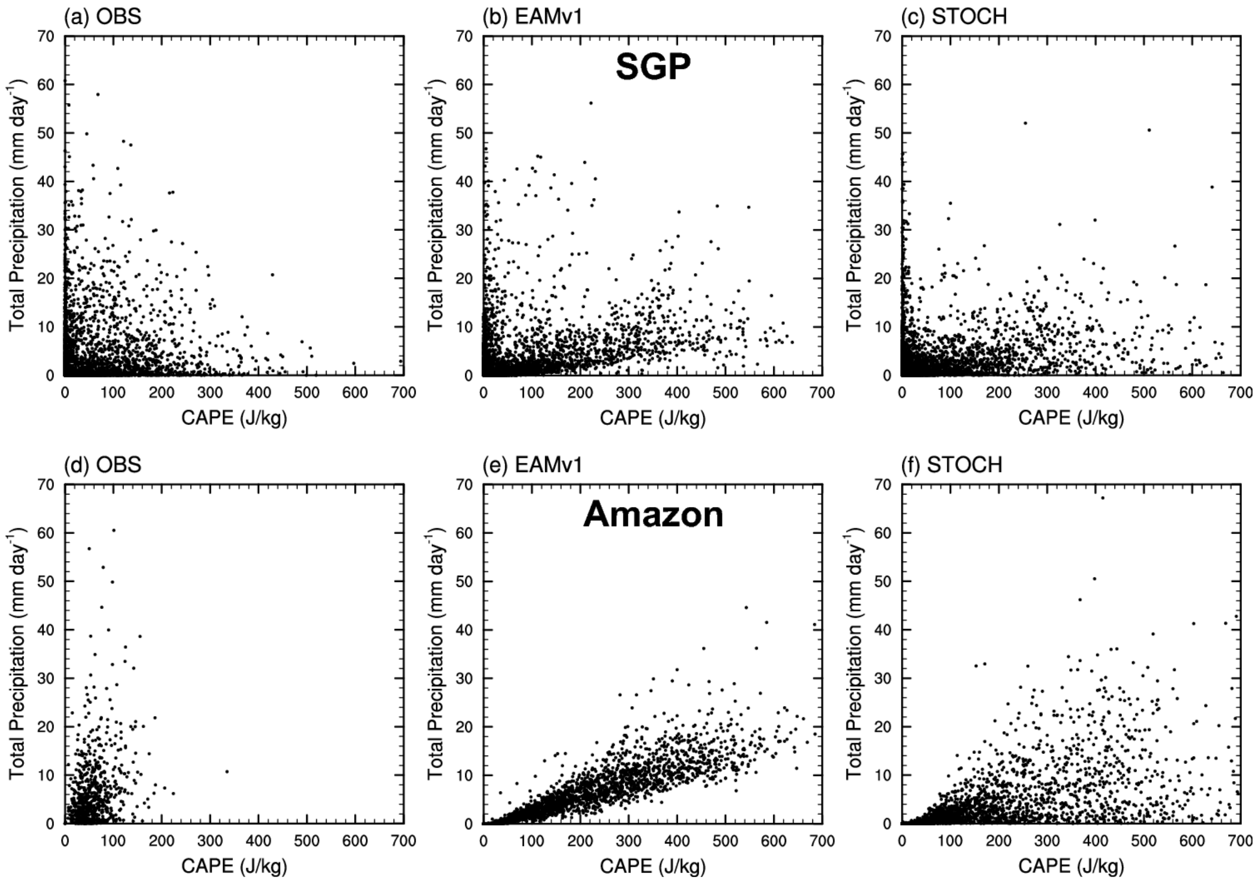

Figure 10. Scatterplots of total precipitation versus CAPE at the ARM (a-c) SGP and (d-f) Amazon sites for (a & d) observations calculated from multi-year sounding data (2014-2015 for Amazon and 2004-2018 for SGP), (b & e) EAMv1 and (c & f) STOCH.

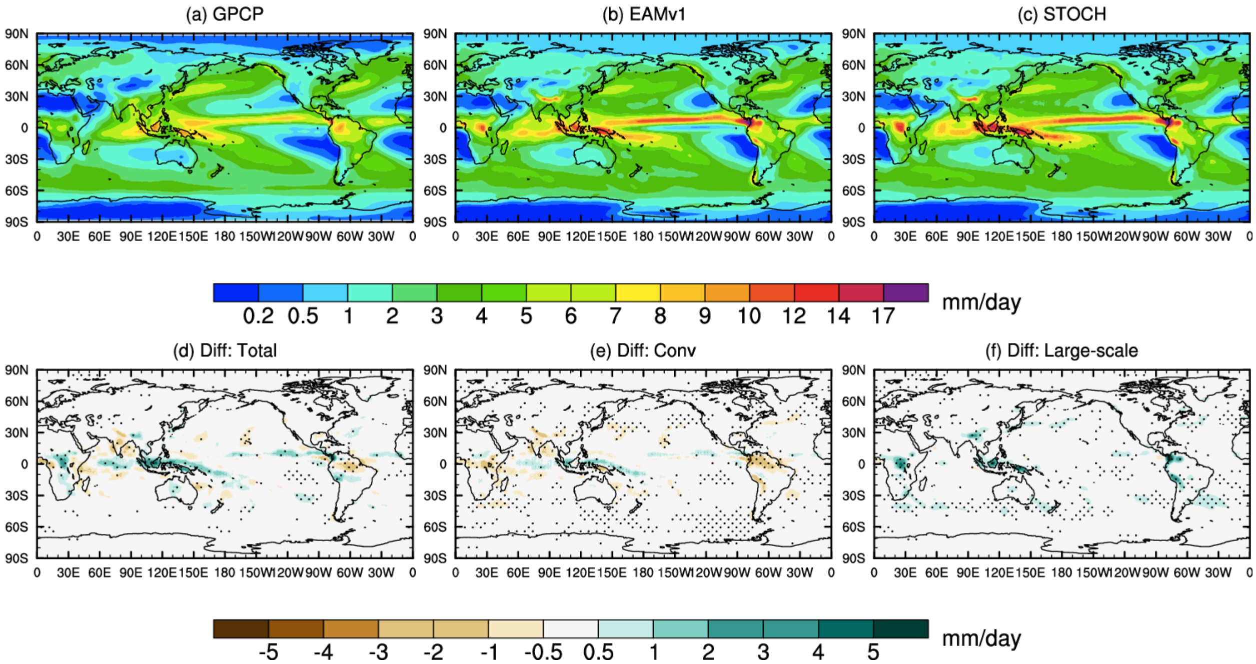

Figure 11. Global distributions of total precipitation for (a) GPCP, (b) EAMv1, and (c) STOCH, and differences of (d) total, (e) convective and (f) large-scale precipitation between STOCH and EAMv1. Differences with a confidence level greater than 95% in (d-f) are stippled.

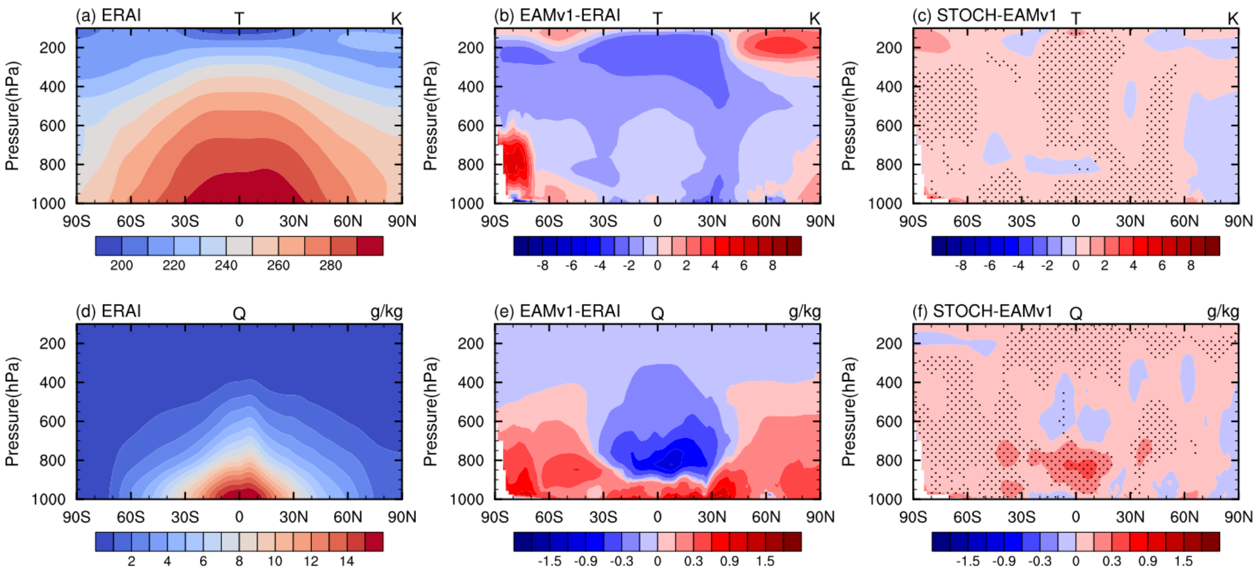

Figure 12. Annual and zonal mean cross sections of (a-c) temperature and (d-f) specific humidity for (a & d) ERAI and differences for (b & e) EAMv1-ERAI and (c & f) STOCH-EAMv1. Differences with a confidence level greater than 95% in between STOCH and EAMv1 are stippled.

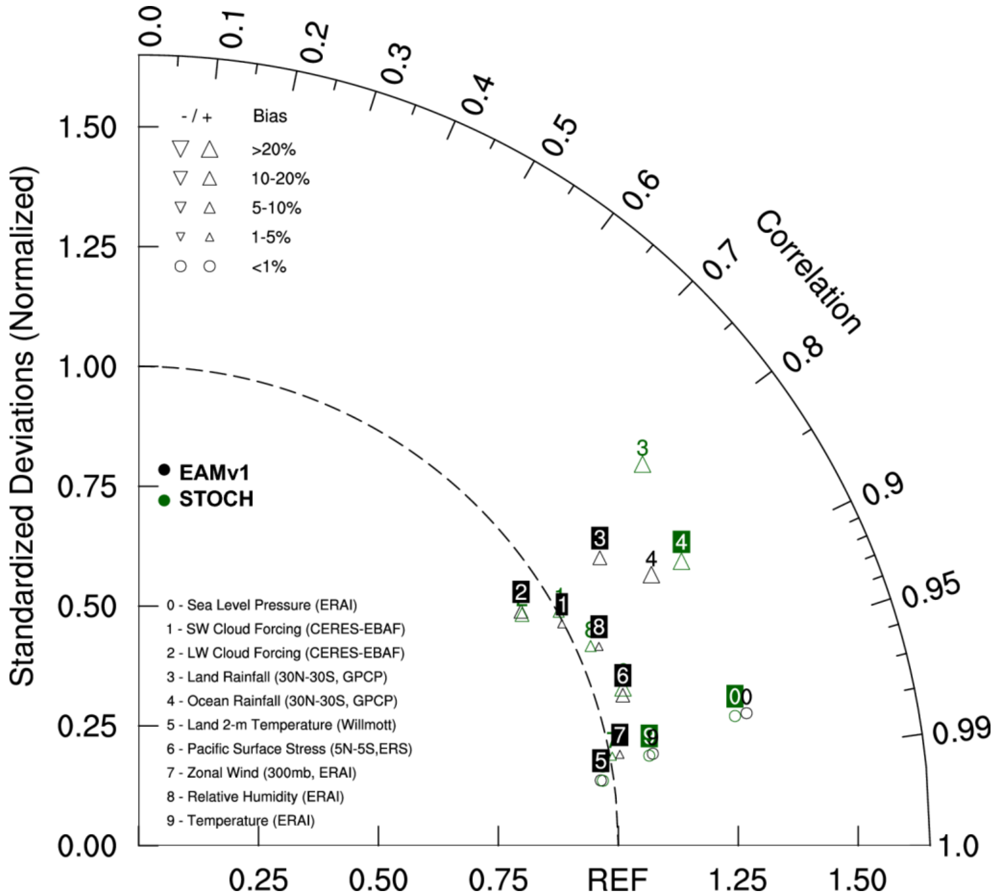

Figure 13. Taylor diagram with metrics for STOCH, compared with EAMv1.

944
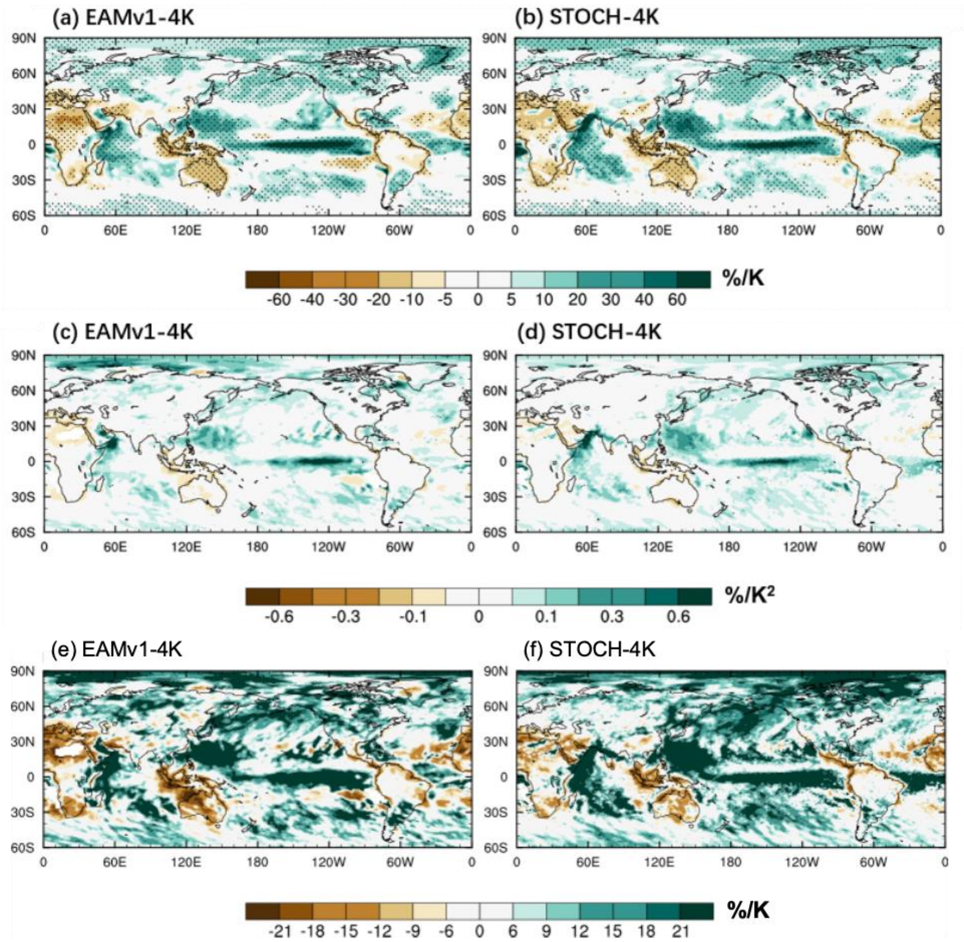

945 **Figure 14.** Geographical distributions of responses of (a & b) annual mean precipitation, (c & d)
946 the coefficient *a*, and (e & f) the fractional change in precipitation extremes (R95p) to climate
947 warming from +4K experiments. Differences with a confidence level greater than 95% are
948 stippled.